Synoptic-Scale and Mesoscale Environments Conducive to Forest Fires during the October 2003 Extreme Fire Event in Southern California

Chenjie Huang

NOAA/NWS/NCEP/Climate Prediction Center, Camp Springs, Maryland, and Wyle Information Systems, McLean, Virginia

Y.-L. Lin

Department of Physics, North Carolina Agricultural and Technical State University, Greensboro, North Carolina

M. L. Kaplan

Division of Atmospheric Sciences, Desert Research Institute, Reno, Nevada

J. J. Charney

North Central Research Station, USDA Forest Service, East Lansing, Michigan

ABSTRACT

This study has employed both observational data and numerical simulation results to diagnose the synoptic-scale and mesoscale environments conducive to forest fires during the October 2003 extreme fire event in southern California. A three-stage process is proposed to illustrate the coupling of the synoptic-scale forcing that is evident from the observations, specifically the high pressure ridge and the upper-level jet streak, which leads to meso-α-scale subsidence in its exit region, and the mesoscale forcing that is simulated by the numerical model, specifically the wave breaking and turbulence as well as the wave-induced critical level, which leads to severe downslope (Santa Ana) winds. Two surges of dry air were found to reach the surface in southern California as revealed in the numerical simulation. The first dry air surge arrived as a result of moisture divergence and isallobaric adjustments behind a surface cold front. The second dry air surge reached southern California as the meso-α- to meso-β-scale subsidence and the wave-induced critical level over the coastal ranges phased to transport the dry air from the upper-level jet streak exit region toward the surface and mix the dry air down to the planetary boundary layer on the lee side of the coastal ranges in southern California. The wave-breaking region on the lee side acted as an internal boundary to reflect the mountain wave energy back to the ground and created severe downslope winds through partial resonance with the upward-propagating mountain waves.

1. Introduction

It has come to fire meteorologists' attention that a significant number of large fires and blow-up fires occur under certain specific synoptic weather patterns. For example, Schaefer (1957) summarized the relationship between jet streams and 23 large fires that occurred in the western United States during the 1955 and 1956 fire seasons, and found that most of the large fires were accompanied by a ''sweeping'' jet stream pattern, in which a high-level jet stream maximum seems to pivot in a region several hundred miles or more up- or downstream from the fire location. This scenario suggests large fires occur in the vicinity of a single jet stream propagating within an upper-level ridge or trough system. Conversely, Schaefer found that only a few of these fires were under the influence of ''conflicting'' jet streams, in which two intense jet streams conflict at upper troposphere indicating the merger of two upper-level jet streams, possibly between a polar jet stream and a subtropical jet stream resulting in strong upper-level

Corresponding author address: Ms. Chenjie Huang, NOAA/CPC and Wyle Information Systems, 1651 Old Meadow Rd., McLean, VA 22102.
E-mail: chenjie.huang@noaa.gov

convergence. Brotak and Reifsnyder (1977a) examined 52 major wildland fires ("major" fires being those that burned more than 5000 acres) in the eastern half of the United States and found that 75% of these fires occurred immediately behind or just ahead of surface cold fronts downstream from small-amplitude but intense 500-hPa short-wave troughs.

It has been recognized that prevailing near-surface weather conditions or the atmospheric planetary boundary layer conducive to erratic fire behavior, including large lapse rates, high temperatures, low humidity, dry fuel, and relatively light winds aloft, are associated with blow-up conditions. Byram (1954) states that for the greatest blow-up potential the wind should reach a maximum within the first 1000 ft (300 m) above the fire and then decrease in speed with elevation for the next several thousand feet. This is equivalent to a low-level jet. Small (1957) analyzed the concurrent weather conditions during the Robie Creek fire in the Boise, Idaho, National Forest, during 5–9 September 1955 and found that Byram's (1954) wind speed profiles offer an explanation for generic fire behavior. However, Brotak and Reifsnyder (1977b) found that Byram's (1954) model tends to explain only buoyancy or convection-driven fires. They analyzed 60 fires in the eastern United States and found that these fires were primarily driven by strong surface winds and that convection above the fire was usually not as important. Kondo and Kuwagata (1992) discovered that forest fires could be enhanced by atypically strong dry winds from the surface up to the lower troposphere that developed shortly after the nocturnal stable boundary layer dissipated as a result of daytime surface heating or synoptic upper-level cold-air advection.

An extreme and devastating "firestorm" happened in southern California in late October 2003. The fires were caused by human intervention and made worse by the Santa Ana winds. There were a total of 14 significant blazes that occurred between 25 October and 2 November 2003. The fires were the second deadliest in California's history. There were 22 people killed and 225 injured. Over 15 000 firefighters participated in the fire suppression. Nearly 750 000 acres of land were burned. The fire caused billions of dollars in damage and about $120 million dollars in suppression costs. More than 3600 residences, 36 commercial buildings, and 1169 outbuildings were destroyed. The time period, on which we will focus for this case study, is from 25 to 27 October 2003. This period was selected because the most dominant fire, the Cedar fire near San Diego (Fig. 1), which was the biggest fire in the state's history and had the greatest damage to property and lives among the fires, developed in the late afternoon on 25 October. Selecting such a focused time period makes it possible to analyze the weather conditions both before and after the fire broke out.

Key to the aforementioned time period is the Santa Ana winds. A Santa Ana wind is a seasonal dry, hot gusty wind with surface wind speeds higher than 13 m s^{-1} in southern California that blows from the northeast through the canyons toward the coasts (Glickman 2000). These winds typically occur during fall to spring and are often observed during the southern California fires. Figure 2 depicts the surface weather map at 1200 UTC 25 October 2003 retrieved from the Service Records Retention System (SRRS) of the National Climatic Data Center (NCDC). Evident is the high pressure system over the Great Basin area juxtaposed near a low pressure system off the southern California coast. The primary surface winds over southern California are northeasterly or easterly. The air immediately preceding the cold front over Arizona as well as just behind the cold front over Nevada and Utah is very dry. For example, the dewpoint depression was as high as 28°C. Such a surface pattern prevailed from 24 to 27 October (Johnson 2004). These features are consistent with published characteristics of Santa Ana winds (e.g., Raphael 2003), and the description of the weather as a Santa Ana event during these southern California fires in October 2003 was forecasted and recorded both at the Storm Prediction Center and at the National Weather Service Weather Forecast Offices in Los Angeles and San Diego (Johnson 2004).

The Santa Ana wind is a type of foehnlike downslope windstorm. There are some conceptual models and/or theories on how downslope wind forms. Eliassen and Palm (1960) and Klemp and Lilly (1975) proposed that downslope windstorms occur when upward-propagating gravity waves are partially reflected by layers in the atmosphere where the Scorer parameter changes rapidly (known as "critical levels"). The reflected energy due to the critical levels results in an optimal superposition of upward- and downward-propagating waves resulting in a downslope windstorm. Others compare downslope windstorm formation to hydraulic jumps employing shallow water theory (Durran 1990). Assuming a homogeneous fluid bounded by a free surface is in hydrostatic balance and flow over a mountain, when the Froude number ($F_r^2 = u^2/gD$) equals 1, the supercritical fluid flow on the windward side transits to subcritical flow at the crest, and the fluid continues to accelerate on the leeward side. Finally, the flow undergoes a hydraulic jump to conform to the ambient downstream conditions. Clark and Peltier (1984) suggested a resonant amplification mechanism in which they proposed that wave breaking above a mountain produces severe windstorms or a high-drag state beneath
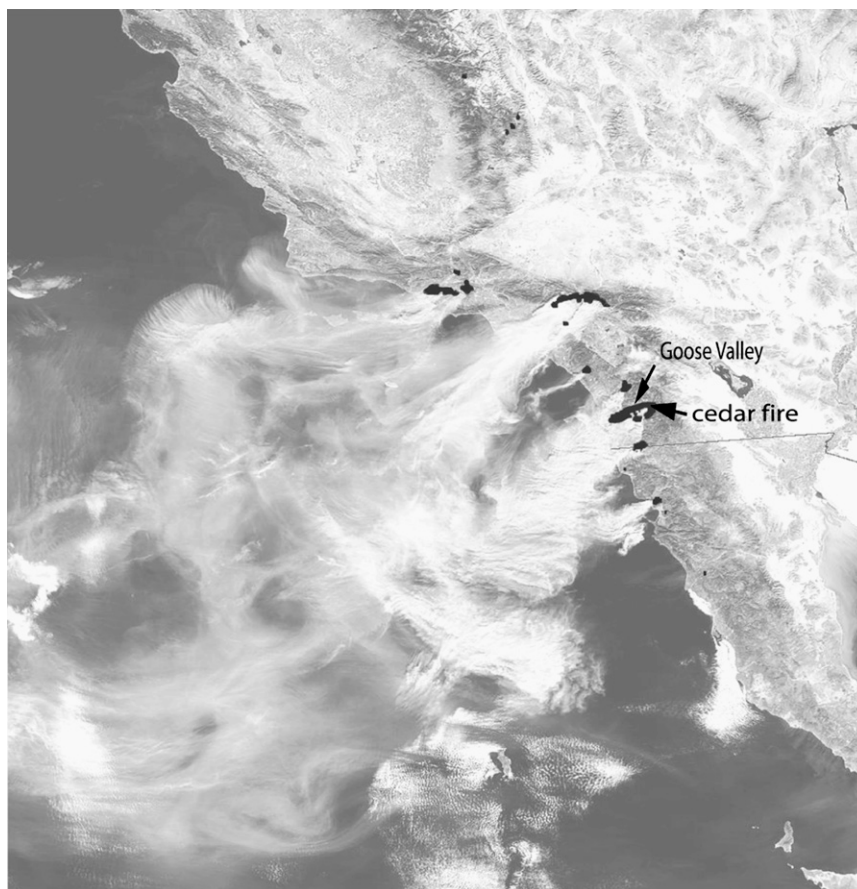
FIG. 1. MODIS satellite image of southern CA fires at 1840 UTC 26 Oct 2003. Arrows pinpoint the cedar fire and the location of Goose Valley, CA. Black spots and shadings denote the fire locations.

a wave-induced critical level. Small (1995) suggested that in the case of a Santa Ana wind, it is possible that the critical layer is not produced by a breaking wave but by an evolving synoptic pattern. In this study, however, it is not our point to argue against or support any one of these theories even if there is similarity among them and our case study, because we are only looking at one event. Neither will we focus on how Santa Ana winds are produced or if this event was different from numerous past events. Santa Ana winds were only a component of the bigger picture, that is, how the atmospheric environment affecting fire development in this particular case study was organized by a multiscale sequence of adjustments.

One may speculate that the Sierra Nevada in southern California would play a role in this process, especially in the production of Santa Ana winds. It is very possible that the upstream mountains affect the formation of Santa Ana winds or the weather dynamics that preceded the Santa Ana event. However, we will not discuss the role of these mountains here due to the limit of this

study. Rather, we will focus on demonstrating what kinds of synoptic- to mesoscale environments are conducive to forest fires and how, in this case study, Santa Ana winds are an outgrowth of a synoptic- to mesoscale sequence of adjustment processes conducive to fire development.

The upper-level flow pattern during this event on the 300-hPa surface was characterized by a jet streak with a core of 50 m s^{-1} or greater wind speed on the northeast periphery of a Pacific high pressure ridge upstream of an intense trough system over the central continental United States (Figs. 3a–d). Such a jet streak is analogous to the ''sweeping'' type jet stream in Schaefer's (1957) study and southern California is under the jet's right exit region. The synoptic-scale patterns, that is, the developing short-wave trough and the rapidly building near-surface high over the Great Basin, are similar to that found in Small's (1995) study on Santa Ana winds.

The 300-hPa horizontal velocity convergence analyses (Figs. 4a–c) show that upper-level convergence
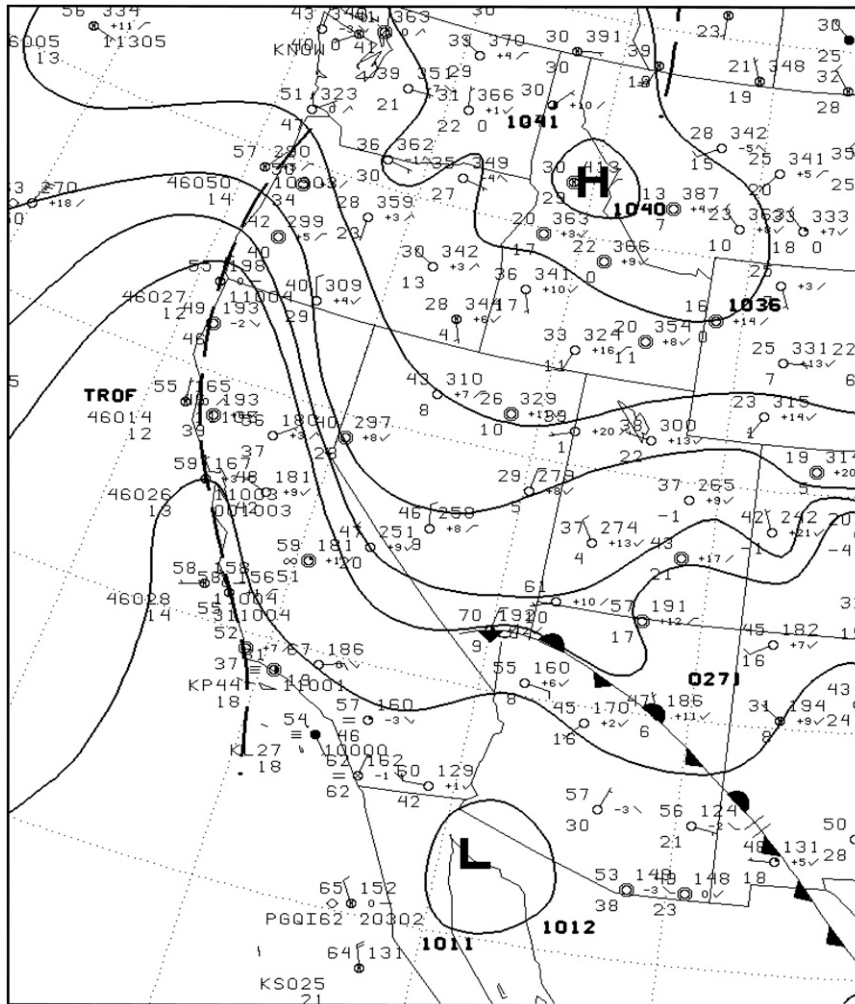
FIG. 2. Surface weather map valid at 1200 UTC 25 Oct 2003. (Figure courtesy of NCDC/SRRS.)
Fire locations are along the southern CA coast.

dominates southern California from 1200 UTC 25 October to 1200 UTC 26 October and the convergence strengthens in time. The upper-level mass flux convergence causes meso-α-scale subsidence over southern California. We hypothesize that this meso-α-scale subsidence has coupled with the low-level atmospheric environments to create extremely dry and gusty conditions on the lee side of coastal ranges in southern California, thus contributing to the formation of Santa Ana winds, making the fire suppression processes extremely difficult.

This study will investigate the above-hypothesized coupling mechanisms between the upper-level subsidence and low-level atmospheric processes in southern California, using both observational data and numerical simulations. The paradigm derived from this case study may be applied to the complex mountainous region in the western United States. In section 2, we will analyze

the synoptic-scale environment accompanying this southern California fire event during the period from 0000 UTC 25 October to 0000 UTC 27 October 2003 using observational data. Section 3 will describe the numerical model experiment and a brief model validation. Section 4 will present the modeling results and in-depth analyses of the atmospheric dynamics that causes such a widespread hazardous fire disaster. Section 5 will summarize the results.

2. Synoptic-scale environment: Observational analysis

The Barnes analysis scheme is used to examine the synoptic-scale environment of the observational data, such as rawinsonde soundings and surface aviation observations, preceding the southern California fires of
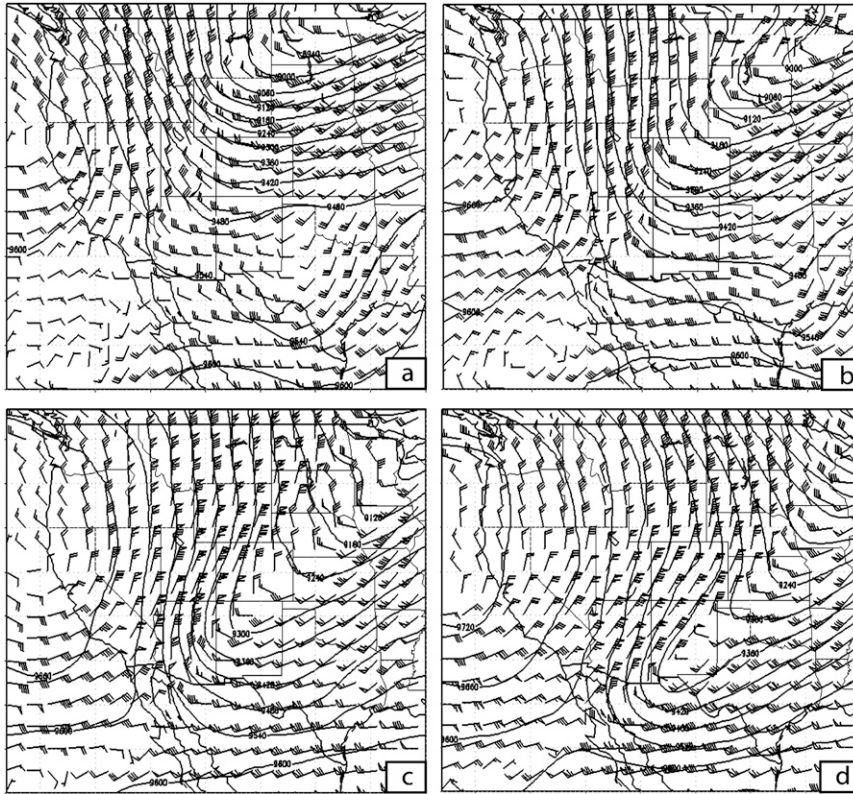
FIG. 3. North American Regional Reanalysis (NARR) data of 300-hPa geopotential height (solid; m) and wind barbs valid at (a) 0000 UTC 25 Oct, (b) 1200 UTC 25 Oct, (c) 0000 UTC 26 Oct, and (d) 1200 UTC 26 Oct 2003. A long (short) wind barb denotes 10 (5) kt. A flag denotes 50 kt.

October 2003. Figures 5a–f denote the 300- and 700-hPa height fields and horizontal wind speeds, as well as the surface RH and wind barbs derived from the Barnes analysis of the raw radiosonde dataset, at 0000 UTC 25 October and 1200 UTC 26 October. A positively tilted upper-level trough that was over the northern Great Basin and the northern Great Plains at 0000 UTC 25 October (Fig. 5a) deepened and dug southward toward the southern Great Basin (Fig. 5b). Cold air of polar origin was advected southward to the southwestern United States including Utah, Arizona, Colorado, and New Mexico. As the northern portion of this upper-level trough moved downstream (eastward), the southwestern portion of this trough, however, became anchored over the southwestern states (Fig. 5b). Accompanied by the evolution of the trough was the development of the high pressure ridge over the western U.S. coast. Indicated by the pressure rise of the inner-most contour of the ridge and the movement of the 9660-m height contour over the West Coast and California, the high pressure ridge strengthened and progressed north-northeastward over time.

Concurrently, a 300-hPa jet streak at the northeastern periphery of the high pressure ridge over the northwestern United States and the U.S.–Canada border strengthened with a core of wind speed greater than 60 m s^{-1} and became more anticyclonically curved in time (Fig. 5b). A smaller-scale (about 500 mi in diameter) jet streak was observed to develop over the southwestern states at 1200 UTC 26 October (Fig. 5b) and weakened 12 h later (not shown).

The major synoptic feature of the lower-tropospheric environment (Figs. 5c and 5d) was the intensification of the high pressure ridge and the jet streak genesis on the northeastern periphery of this ridge. The curvature of the jet streak also tends to increase with time. The surface RH analysis from the surface aviation observations (SAOs) shows that the surface air over southern California and the nearby southwestern states was very dry during this period (Figs. 5e and 5f). The surface RH over most of the southern states was below 20% at 0000 UTC 25 October (Fig. 5e). As the daytime solar heating became stronger, the area where the RH was below 20% was enlarged to most of southwestern states at
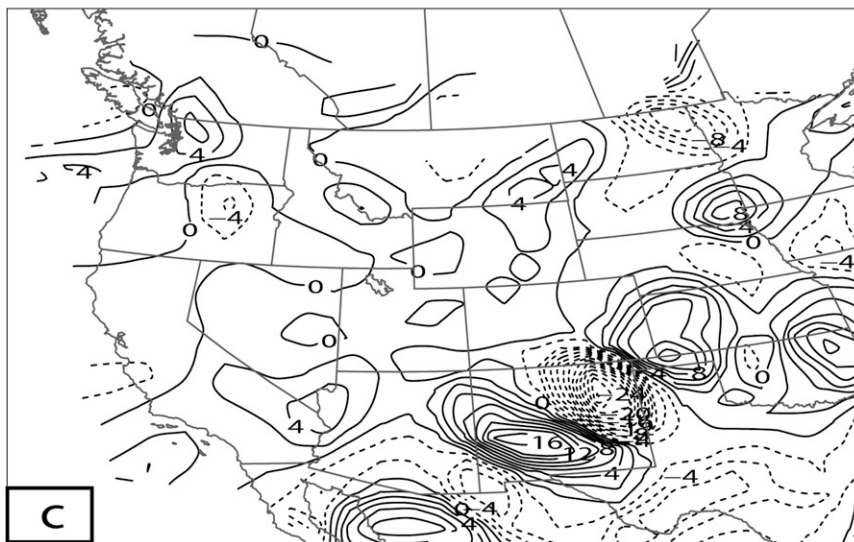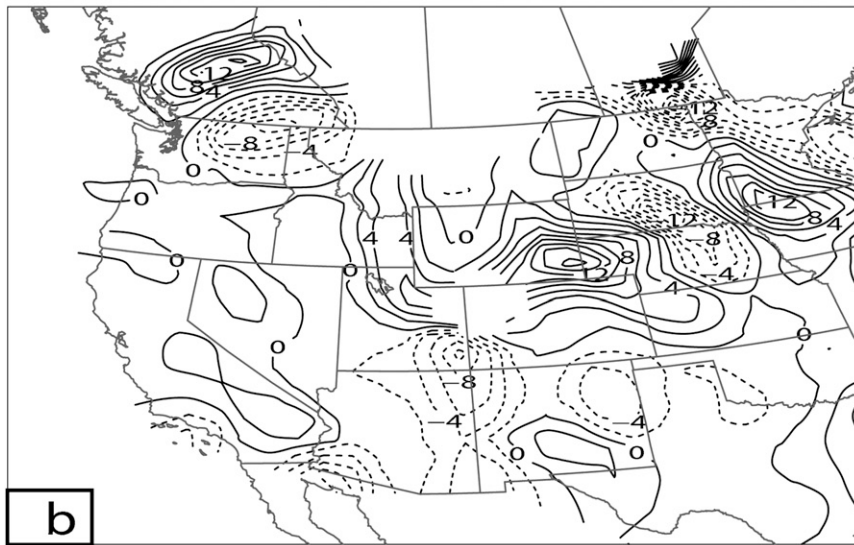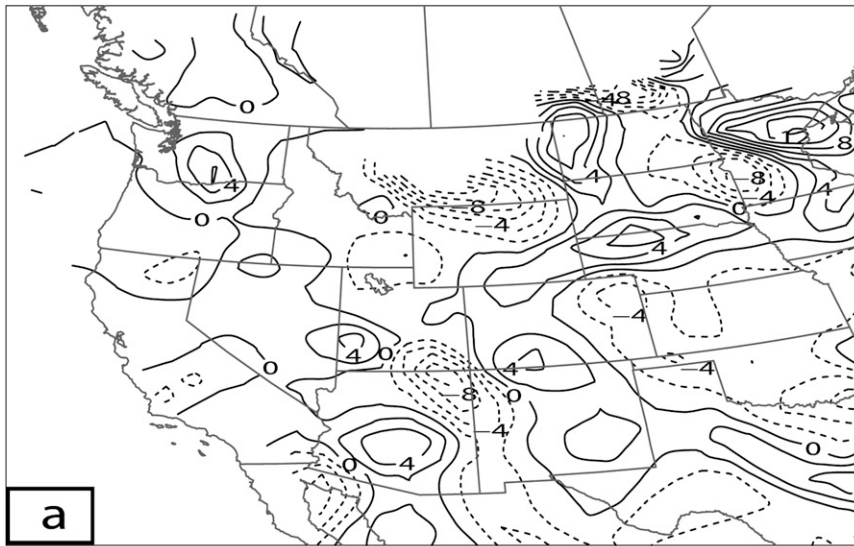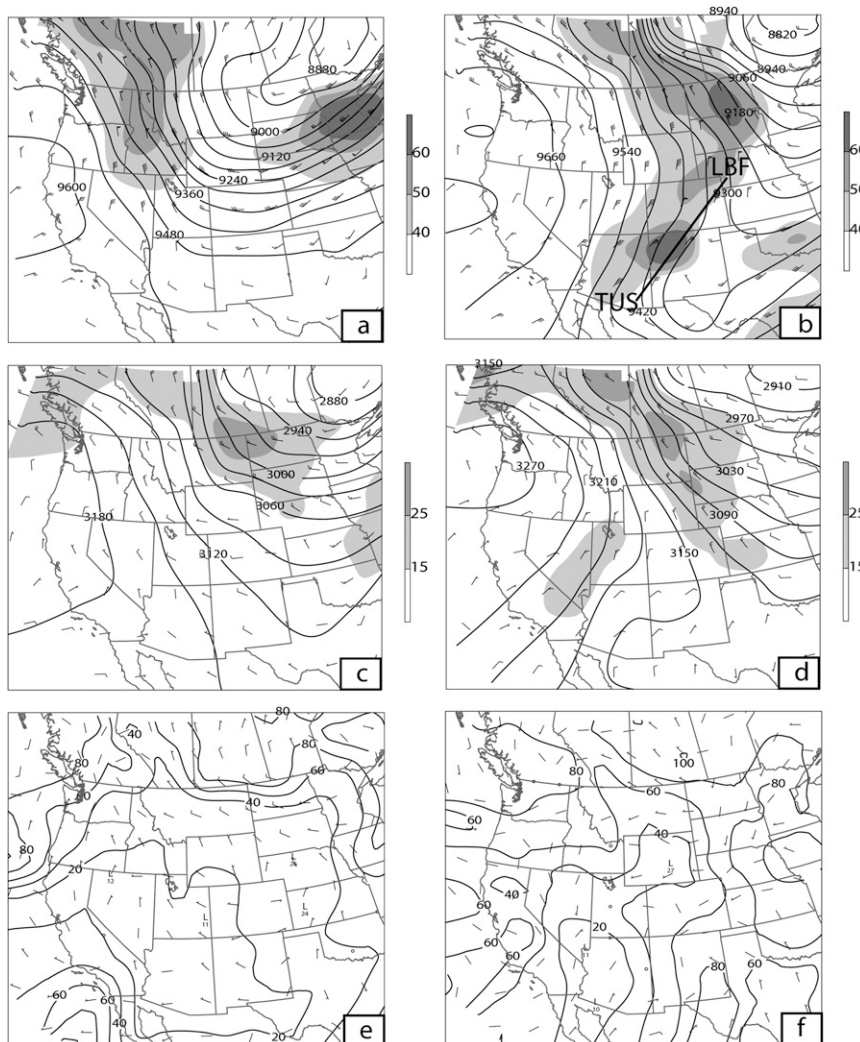
FIG. 5. Barnes analysis of (a),(b) 300- and (c),(d) 700-hPa geopotential height (solid lines; m), wind speed (shaded) and wind barbs, and (e),(f) surface RH (solid lines; %) and wind barbs valid at (left) 0000 UTC 25 Oct and (right) 1200 UTC 26 Oct 2003. A long (short) wind barb denotes 10 (5) m s^{-1}. A flag denotes 50 m s^{-1}. Boldface solid line in (b) denotes cross-section location in Fig. 9.

0000 UTC 26 October (not shown) and remained below this value over southern California, southern Nevada, and western Arizona (Fig. 5f).

High-resolution Remote Automated Weather Stations (RAWS) data over Goose Valley, California (see Fig. 1 for its location), recorded single-digit RH at 1200 UTC [0400 local standard time (LST)] 26 October, which lasted through the day (Fig. 6a). Air temperatures climbed to ~35°C in the late morning of 25 October and

persisted into the afternoon (Fig. 6b). Fuel moisture (RH of the fuel on the ground) dropped down to below five units during the entire period spanning 0000 LST 25 October–0000 LST 27 October (Fig. 6c). In the meantime, the gusty surface wind speed reached >17 m s^{-1} at 1400 UTC (0600 LST) 26 October (Fig. 6d). Similar anomalously hot, dry, and gusty wind conditions were found in nearby stations where the fire "blew up" into an erratic firestorm.

←

FIG. 4. The 300-hPa convergence (10^{-5} s^{-1}) (positive, solid contours; negative, dashed contours) derived from Barnes analyses of radiosonde observational data valid at (a) 1200 UTC 25 Oct, (b) 0000 UTC 26 Oct, and (c) 1200 UTC 26 Oct 2003.
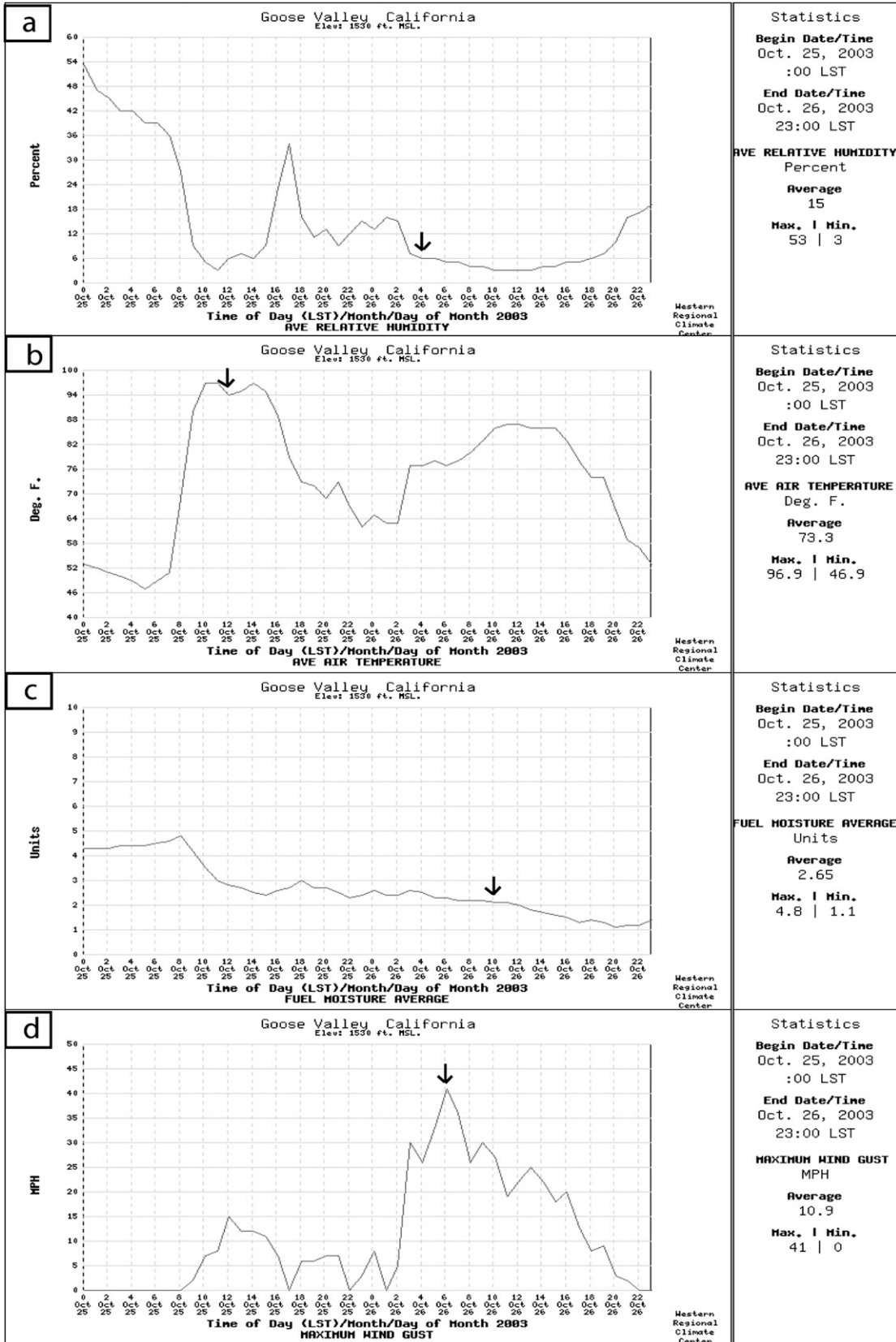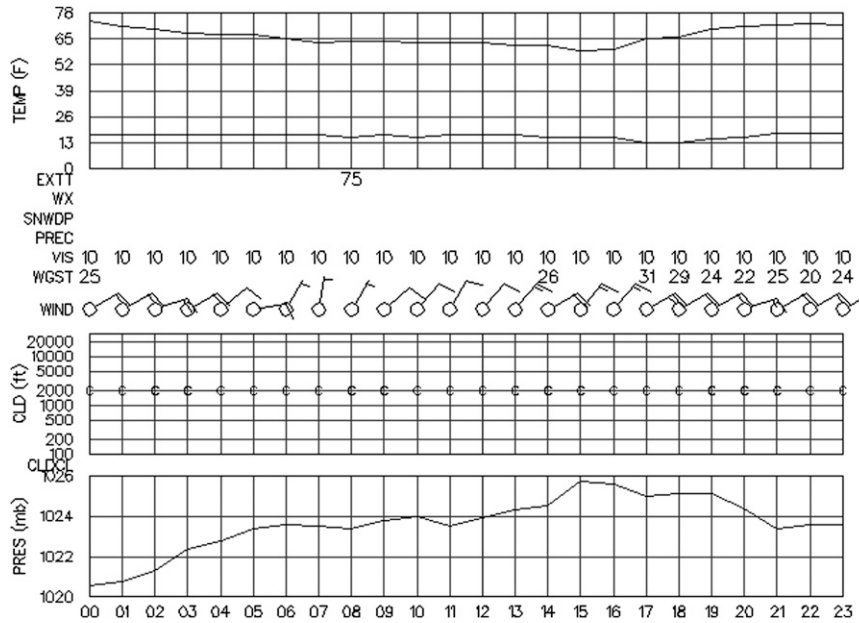
FIG. 7. Meteogram for KSDB from 0000 to 2300 UTC 26 Oct 2003.

The meteogram for Sandburg, California (KSDB), from 0000 to 2300 UTC 26 October 2003 (Fig. 7), also depicts a surface dewpoint depression of ~20°C or greater, indicating very dry surface conditions, a prevailing northeasterly wind of 5 m s^{-1} with 10 m s^{-1} or greater wind gusts under a clear sky with visibility of 10 mi, and a steady pressure rise during the local afternoon of 25 October to the morning (until 1500 UTC) of 26 October, indicating horizontal convergence or descending air motion throughout a substantial portion of the air column.

The rawinsonde-derived thermodynamic diagram for Miramar, California (KNKX; Fig. 8), at four different times from 0000 UTC 25 October to 1200 UTC 26 October 2003 showed common characteristics of the sounding near the fire site: a temperature inversion layer near the surface below 900 hPa with a nearly dry-adiabatic layer above it, a very dry layer in the lower troposphere with the drying becoming enlarged in time, and the wind direction reversing in the lower atmosphere indicating a possible wave-induced critical level (e.g., Lin 2007). The role of this critical level in producing severe downslope winds on the lee side of coastal ranges near San Diego, California, will be investigated in detail in section 3.

The analyzed RH, potential temperature, and wind barbs in the cross section from the Tucson, Arizona, International Airport (TUS), to North Platte, Nebraska

(LBF), valid at 1200 UTC 26 October (Fig. 9a), denote that a deep layer of extremely dry air with RH < 10% has reached the lower troposphere below 500 hPa in between TUS and Albuquerque, New Mexico (ABQ). Northeasterly winds of 35 m s^{-1} or greater are recorded at these levels. Three fronts can be identified from the packing and sloping of the isentropes: 1) the upper-level front indicated by the 326–320-K isentropes encompassing the layer of 300–370 hPa in between TUS and ABQ; 2) the middle-level front in the layer spanning the 316 K–302-K isentropes located in between TUS and ABQ, and the 308–302-K isentropes above DNR; and 3) the boundary layer front in between the 298–294-K isentropes above ABQ.

3. Mesoscale numerical simulations

a. Model description

The mesoscale modeling system used here is the Mesocale Atmospheric Simulation System (MASS). MASS is a limited-area terrain-following sigma-coordinate model that can be run either in hydrostatic or nonhydrostatic mode and is designed to simulate or predict mesoscale and regional-scale atmospheric circulations. The version used here is nonhydrostatic (NHMASS) version 6.3

←

FIG. 6. Automated Surface Observing System (ASOS)-recorded time series of surface (a) air RH (%), (b) air temperature (°F), (c) fuel moisture (%), and (d) gusty wind speed (mi h^{-1}) at Goose Valley from 25 Oct to 27 Oct 2003. Arrows define key times discussed in the text.
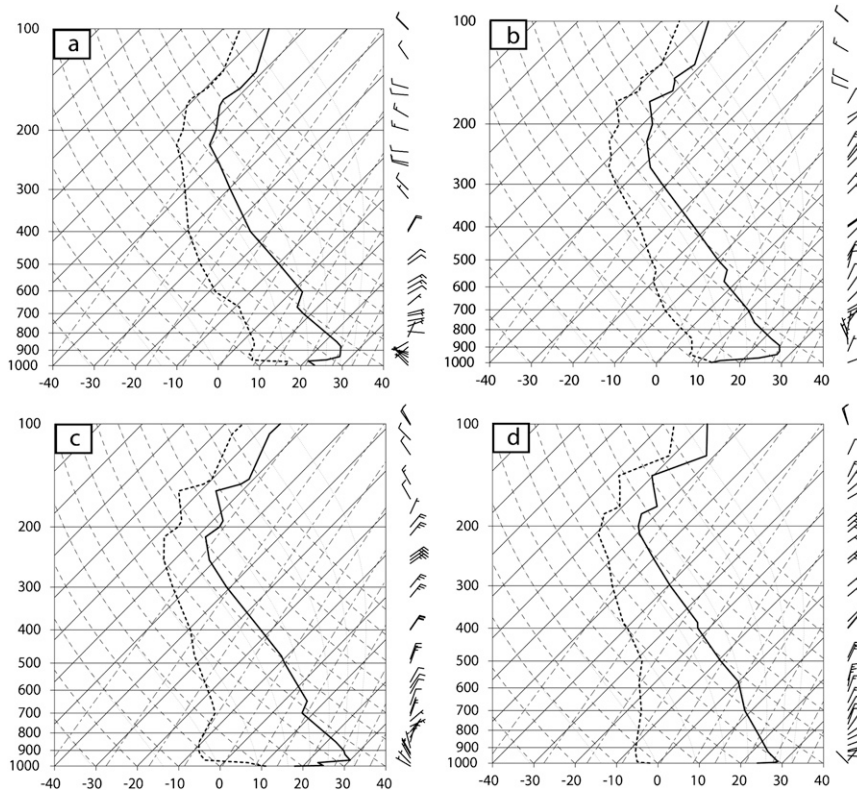
FIG. 8. Observed thermodynamic diagrams for KNKX valid at (a) 0000 UTC 25 Oct, (b) 1200 UTC 25 Oct, (c) 0000 UTC 26 Oct, and (d) 1200 UTC 26 Oct 2003. Solid line denotes temperature and dashed line denotes dewpoint temperature.

(Kaplan et al. 2000; MESO, Inc. 1994). NHMASS 6.3 has interactive multiple-nest capability, nonhydrostatic dynamics allowing simulations on the order of 1 km or finer, a four-dimensional data-assimilation capability, and several microphysics as well as convective parameterization schemes.

NHMASS 6.3 has three map projection options and the polar stereographic map projection is used here since the interest area is in the middle to high latitudes. Variable resolution for various surface characteristic data, such as terrain elevation, land–water differentiation, land use, soil type, and vegetation density, are available with this version of the model and are employed here. One-way grid nesting was employed in this study. The National Centers for Environmental Prediction–National Center for Atmospheric Research (NCEP–NCAR) reanalysis dataset is utilized to initialize the numerical model and produce time-dependent lateral boundary conditions.

b. Experimental design

Figure 9b denotes the three domains used in this study, including domain 1 with a coarse grid spacing of 32 km, domain 2 with a grid spacing of 8 km, and do-

main 3 with a grid spacing of 2 km. Domain 1 covers the western United States and part of Canada, aiming to reproduce the synoptic flow pattern in which the mesoscale environment is embedded. Domain 2 includes the southwestern states such as California, Nevada, Utah, and Arizona. Domain 3 focuses on capturing meso-β-scale characteristics of the flow over southern California, where the fire was the most destructive. To capture the very finescale vertical motions, all three model runs contain 59 σ–p vertical levels (with a model top at about 100 hPa), among which approximately 30 levels are within the planetary boundary layer. All three control runs have full physical processes turned on.

The grid points for each model run are, in the x–y direction, respectively, 100 $\times$ 110 for domain 1, 174 $\times$ 174 for domain 2, and 200 $\times$ 200 for domain 3. Domain 1 is initialized with the routine upper-air and surface aviation observational data at 0000 UTC 25 October 2003 and the forecast period is 48 h, ending at 0000 UTC 27 October 2003. Domain 2 is initialized at 1200 UTC 25 October 2003 and run for 36 h, and domain 3 is initialized at 0000 UTC 26 October 2003 and completed at 0000 UTC 27 October 2003. Domains 2 and 3 are
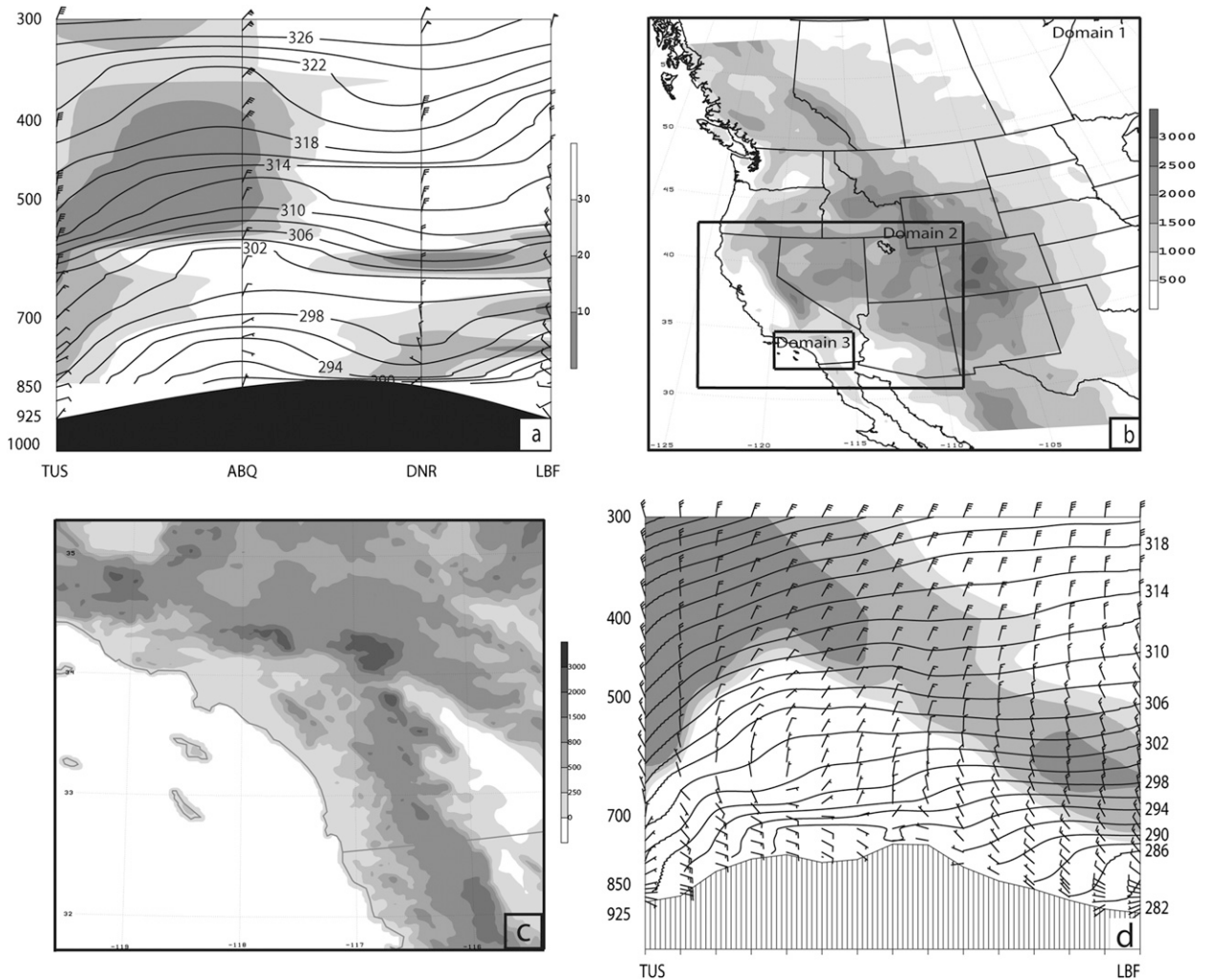
FIG. 9. (a) Analyzed RH (%; lightly shaded for RH < 30%, intermittently shaded for RH < 20%, and heavily shaded for RH < 10%), potential temperature (K), and wind barbs from Barnes analysis valid at 1200 UTC 26 Oct 2003 in the cross section from TUS to LBF (denoted in Fig. 5b). (b) Three domains in the NHMASS simulations and terrain height from domain 1 (shaded; m). (c) The 2-km NHMASS [domain 3 in (b)] terrain height (shaded; m). (d) As in (a), but from the 32-km NHMASS simulation. Wind barb symbols are the same as in Fig. 5.

initialized with model output from domains 1 and 2, respectively. The integration time steps of each model run are automatically determined by the model according to the Courant–Friedrichs–Lewy (CFL) criterion; the time steps are less than 54, 15, and 4 s for domains 1, 2, and 3, respectively.

The Kain–Fritsch cumulus parameterization scheme, turbulent kinetic energy (TKE) boundary layer parameterization scheme, and mixed-phase without hail microphysics scheme have been employed for all the model runs. Table 1 summarizes the specifications of NHMASS model version 6.3 and the various settings used in the simulations performed in this study.

Figure 9c represents the 2-km NHMASS simulated terrain. We can see that the finer-scale terrain features

were well captured in the model. The San Gabriel Mountains and other high peaks over 3000 m were reproduced by the high-resolution terrain database used in the NHMASS model.

c. NHMASS coarse-simulation validation

Figure 9d denotes the 32-km NHMASS simulated cross-section analysis of RH, potential temperature, and total winds across TUS and LBF. The simulation captures the deep dry layer extending from 400 to 600 hPa between TUS and ABQ and the shallower dry layer spanning from 550 to 650 hPa between Denver, Colorado (DNR), and LBF. The pattern of potential temperature and the wind field are simulated reasonably well except that the maximum wind speed in the

TABLE 1. NHMASS version 6.3 model characteristics.

Model numerics
Nonhydrostatic primitive equation model
3D equations for u, v, T, q, and p
Cartesian grid on a polar stereographic map
Sigma-P terrain-following vertical coordinate system
Vertical coverage from ~1 to 16 400 m
Energy-absorbing sponge layer near top of domain
Fourth-order horizontal space-differencing scheme on an unstaggered grid
Split explicit time integration schemes: (a) forward–backward for the gravity mode and (b) Adams–Bashforth for the advective mode
Time-dependent lateral boundary conditions
Positive-definite advection scheme for scalar variables
Massless tracer equations for ozone and aerosol transport
Initialization
First-guess and lateral boundary conditions from NCEP–NCAR Eta Model reanalysis data for the 32-km run and from next
   larger-scale simulation for the 8- and 2-km runs
High-resolution (30 s, 0.5°, or 1 km) terrain database available
High-resolution (30 s, 0.5°, or 1 km) land-use and land cover classification available
High-resolution (30 s, 0.5°, or 1 km) normalized difference vegetation index (NDVI) available
PBL specification
1.5-order TKE PBL parameterization
Surface energy budget
Soil hydrology scheme
Atmospheric radiation attenuation scheme
Moisture physics
Kain–Fritsch cumulus parameterization scheme
Mixed-phase without hail microphysical scheme

simulation is slightly weaker and the upper-level wind over TUS is slightly different from the observational data, that is, the simulation has north-northwesterly flow while the observed wind over TUS is north-northeasterly. This cross section is selected here to validate the model because some sounding data are missing for San Diego. The model may have some weaknesses, however, in simulating the meso-γ- and finer-scale features, upon which this study will not go into details, including how turbulence and downslope winds were affected by the very finescale mountains.

Figure 10 illustrates the 32-km NHMASS simulated regional representation of 300- (Figs. 10a,b) and 700-hPa (Figs. 10c,d) isotachs, height, and wind barbs, as well as surface (Figs. 10e and f) RH (%) and wind barbs (m s^{-1}) valid at 0000 UTC 25 October (Figs. 10a,c, and e) and 1200 UTC 26 October (Figs. 10b,d, and f) 2003. Comparing Fig. 10 with the Barnes analysis in Fig. 5, we see that the NHMASS model is able to reproduce the upper-level flow pattern such as the trough, the high pressure ridge, and the jet streak at the northeastern periphery of the high pressure ridge except that the jet streak is stronger than that in the observations. The total wind direction is simulated very well. The lower-level features are also captured reasonably well except that the mesoscale vortex at 700 hPa over Nebraska and northern New Mexico from the simulation is more obvious than that from the observations (Fig. 10d) and the

surface RH field in the simulation is moister than the observations (Figs. 10e and 10f).

Figure 11 presents a comparison of the thermodynamic diagrams at NKX from the Barnes analyses of the observational data and from the output of the 32-km NHMASS simulation valid at 1200 UTC 25 October and 0000 UTC 26 October 2003. The temperature inversion layer near the surface and the nearly dry-adiabatic layer above it are well simulated by the model. The very dry lower troposphere below 800 hPa is captured as well. The temperature and dewpoint profiles in the simulation are generally consistent with the observations. The wind speed and direction agree with the observations as well, except that the wind reversal level (a possible wave-induced "critical level") is missing at this time in the simulation. An examination of the simulated sounding at a later time (starting at 0300 UTC 26 October 2003) indicates that the model does capture the wind reversal level (not shown). Therefore, the model is slower than the observations, which is quite typical for a limited-region mesoscale modeling system because the model needs some "spinup" time.

4. Simulated synoptic-scale and mesoscale environment

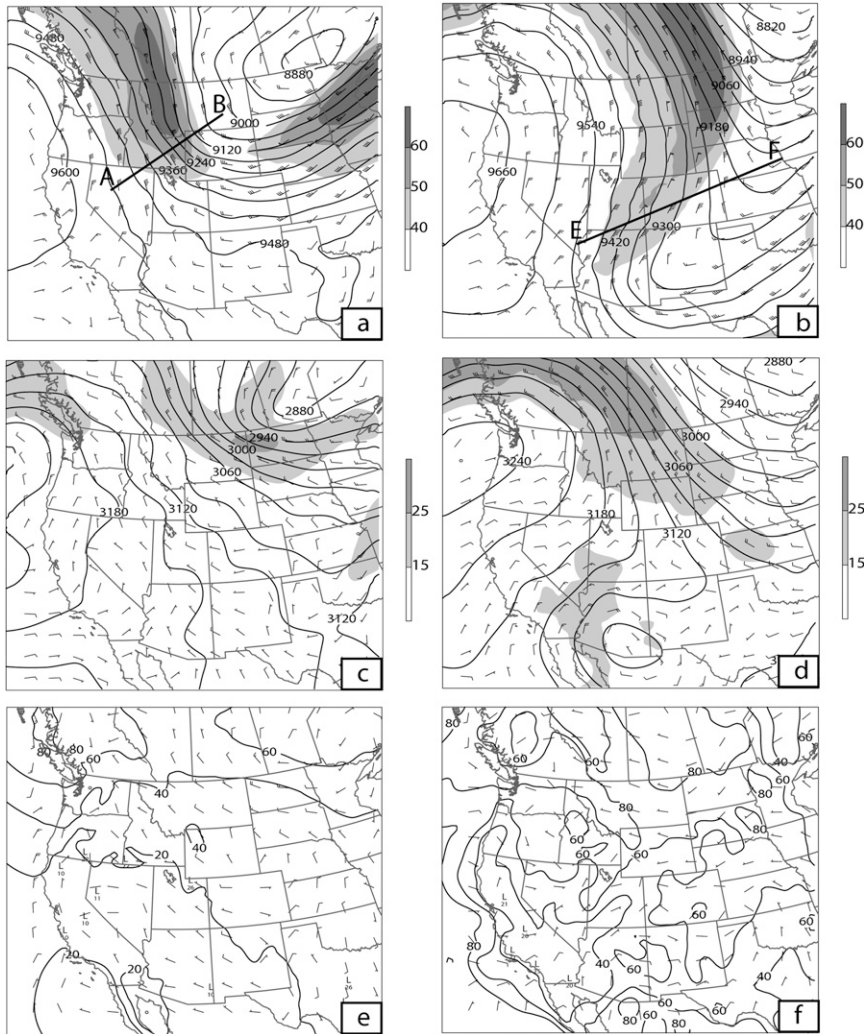Section 2 described a coarse-resolution Barnes analysis of the synoptic-scale environment based on the

FIG. 10. Analysis of (a),(b) 300- and (c),(d) 700-hPa isotachs (shaded; m s^{-1}), geopotential height (solid; m), and wind barbs (m s^{-1}), and (e),(f) surface RH (solid; %) and wind barbs (m s^{-1}) from the 32-km simulation valid at (left) 0000 UTC 25 Oct and (right) 1200 UTC 26 Oct 2003. Wind barb symbols are the same as in Fig. 5. Boldface lines in (a),(b) denote cross-section locations for Figs. 19a and 19c but are valid at 0300 UTC 25 Oct and 1200 UTC 26 Oct, respectively.

observational data. In this section in-depth analyses of the dynamics will be presented from the NHMASS modeling results to explain how the hot, dry, and windy atmospheric environment conducive to large-scale fires developed as a result of the coupling of the synoptic-scale and mesoscale processes.

The polar jet streak upstream of the upper-level trough over the north-central United States strengthened from 0000 UTC 25 October to 1200 UTC 26 October 2003 and evolved from a straight jet into a more anticyclonically curved jet (Figs. 10a and 10b). The increase in curvature has an important impact on the force balance that an air parcel may experience

when passing through the jet streak; that is, the centrifugal force increases as the curvature increases. The sinking branch of the transverse ageostrophic secondary circulation is amplified on the anticyclonic side and the rising branch is suppressed on the cyclonic side due to the increased centrifugal force. Therefore, the sinking motion on and beneath 300 hPa above the western U.S. coast became stronger as the jet streak strengthened and propagated southeastward.

Figure 12 illustrates the vertical motion in the upper, middle, and lower troposphere from the 32-km NHMASS simulation valid at 1200 UTC 25 October and 1200 UTC 26 October. One may note how the subsidence
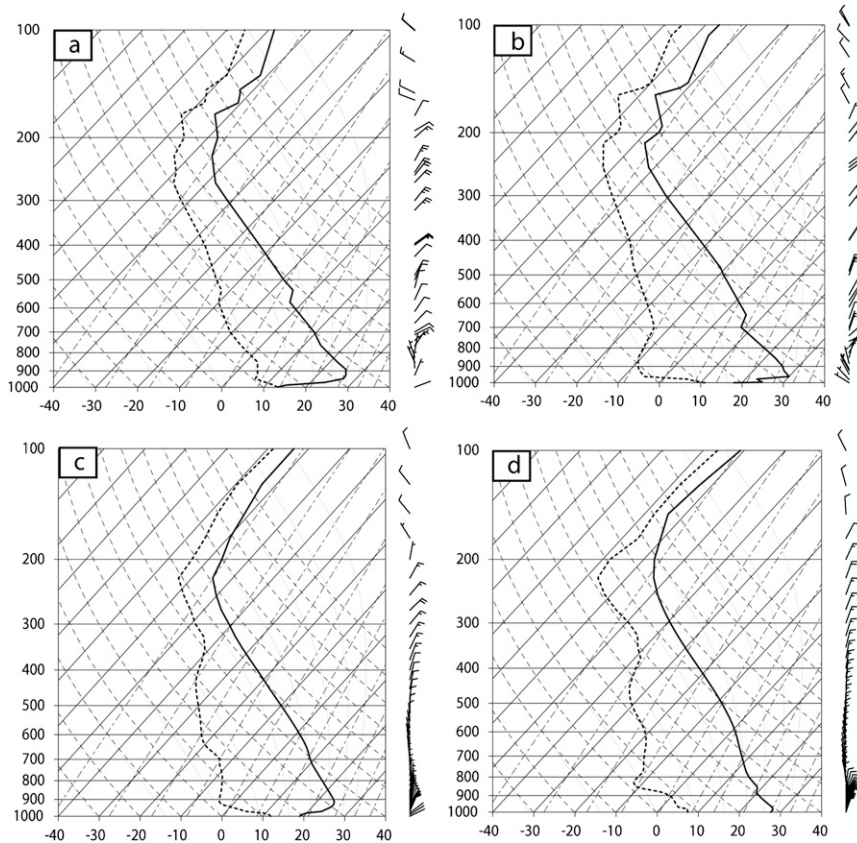
FIG. 11. Thermodynamic diagrams obtained from (a),(b) Barnes analysis of observational data and (c),(d) the 32-km NHMASS simulation valid at (left) 1200 UTC 25 Oct and (right) 0000 UTC 26 Oct 2003.

over Idaho and Utah (Figs. 12a and 12c) strengthened and propagated southward to Arizona and the U.S.–Mexico border (Figs. 12b and 12d). Also note that in the upper and middle troposphere, southern California was always dominated by a mesoscale descending motion (Figs. 12a–d). Another noticeable feature of Fig. 12 is that at 1200 UTC 26 October, the strong upper-, middle-, and lower-level sinking motions over southern California and northeastern Arizona are in phase (Figs. 12b, 12d, and 12f). This phasing will provide strong meso-α- to meso-β-scale forcing to bring the dry high-momentum air from the upper troposphere down to the PBL.

The meso-α-scale sinking motion would also strengthen due to the strong cold air advection at the lower and middle troposphere (Fig. 13). We can see from Figs. 13a and 13c that the wind barbs are almost parallel to the geopotential height contours over the southwestern United States at both the 500- and 700-hPa levels. Therefore, quasigeostrophic (QG) theory still applies, although as the curvature increases, the Eulerian Rossby number also increases as along-flow accelerations increase. One

can see that at 1200 UTC 26 October there was strong cold-air advection over the southwestern United States in the middle to lower troposphere, especially at the 700-hPa level (Figs. 13b–d). Applying the omega equation in QG theory (Holton 2004), we know that Laplacian of cold advection in the lower atmosphere causes sinking motion. Therefore, the sinking motions over these regions will get stronger.

When air parcels turned to the right under the influence of the rightward-directed ageostrophic winds in the exit region of the 300-hPa jet streak (Figs. 13e and 13f) and sank simultaneously before reaching the top of the PBL, their temperatures rose due to adiabatic compression. After these air parcels reached the top of the daytime PBL, warming was more rapid and effective due to the turbulent mixing and the temperature lapse rate that was close to dry adiabatic [about $9.8°C$ $(1000 m)^{-1}$]; that is, a parcel's temperature would increase almost $10°C$ by descending 1 km adiabatically.

Figure 14a depicts backward-trajectory analyses of 24 air parcels from the 32-km coarse simulation released at 850 hPa in southern California at 0000 UTC 27 October,
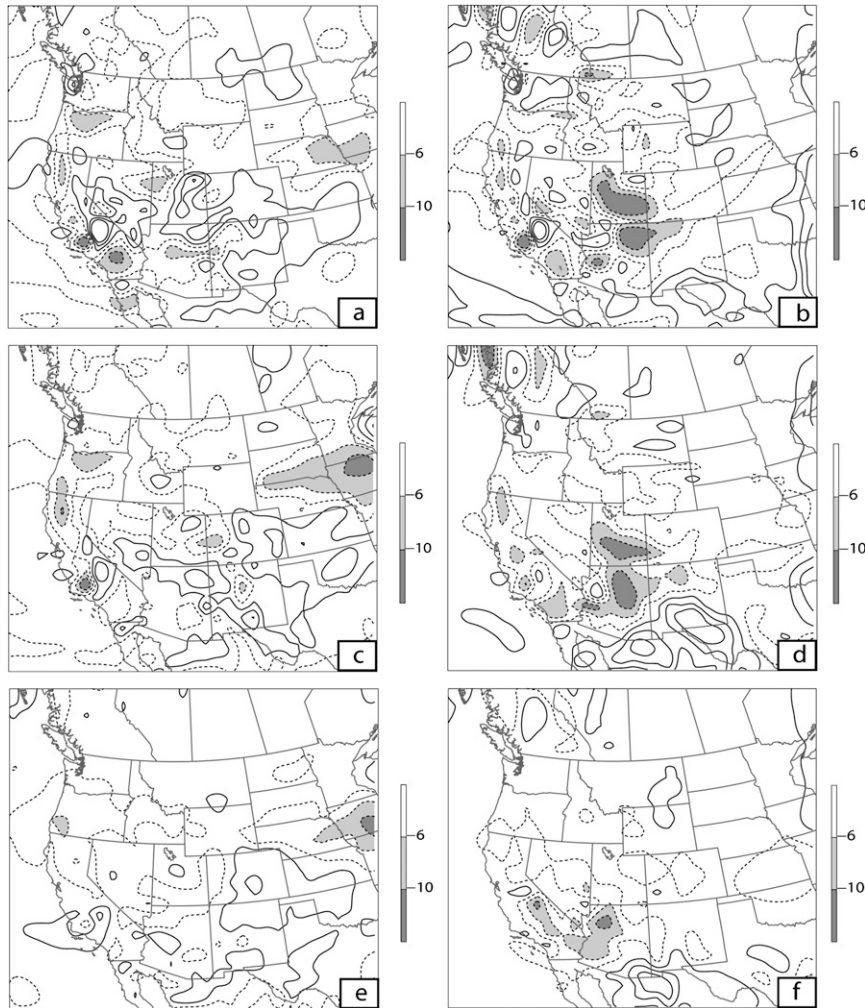
FIG. 12. Vertical velocity (cm s^{-1}) at (a),(b) 300, (c),(d) 500, and (e),(f) 700 hPa from the 32-km NHMASS simulation at (left) 1200 UTC 25 Oct and (right) 1200 UTC 26 Oct 2003. Solid lines denote updraft and dashed lines downdraft. Downdrafts stronger than -6 cm s^{-1} are shaded.

among which three parcels were selected to depict the accompanied dramatic drying and warming (Figs. 14b–d). One can see that the majority of these parcels followed an anticyclonically turning trajectory, which originated over southwestern Canada. Only a few of them were from the central plains (Fig. 14a). As the three selected parcels sank from the mid- to upper troposphere over southwestern Canada down to the lower troposphere over the southern California coast, they all had a dramatic warming from roughly the middle $-30°$Cs at $\sim$400 hPa to roughly the middle 10°Cs at 850 hPa (Figs. 14b–d). The rate of warming was faster after these parcels reached the top of the PBL at 1800 UTC 26 October (Figs. 14b–d). Their temperatures rapidly increased from $\sim$8°C at about 750 hPa to $\sim$16°C at about 835 hPa. Trajectories in Figs. 14b–d also indicated that

these parcels (except parcel C) originated over southwestern Canada in the mid- to upper troposphere and were extremely dry with the RH remaining below 10%. The trajectory of parcel C suggests a drying process as the parcel was forced down toward the surface with an RH of 46% at 395 hPa over southwestern Canada and as it turned into southern California its RH dropped to only 13% at 850 hPa.

Figure 15 denotes the total winds and surface mixing ratios every 12 h from 1200 UTC 25 October to 0000 UTC 27 October from the 32-km simulation. We can see that the main body of the surface dry air approached California from southwestern Canada and the northwestern United States at 1200 UTC 25 October (Fig. 15a) and moved southwestward over southern California 24 h later (Fig. 15c). Ahead of it, some very small
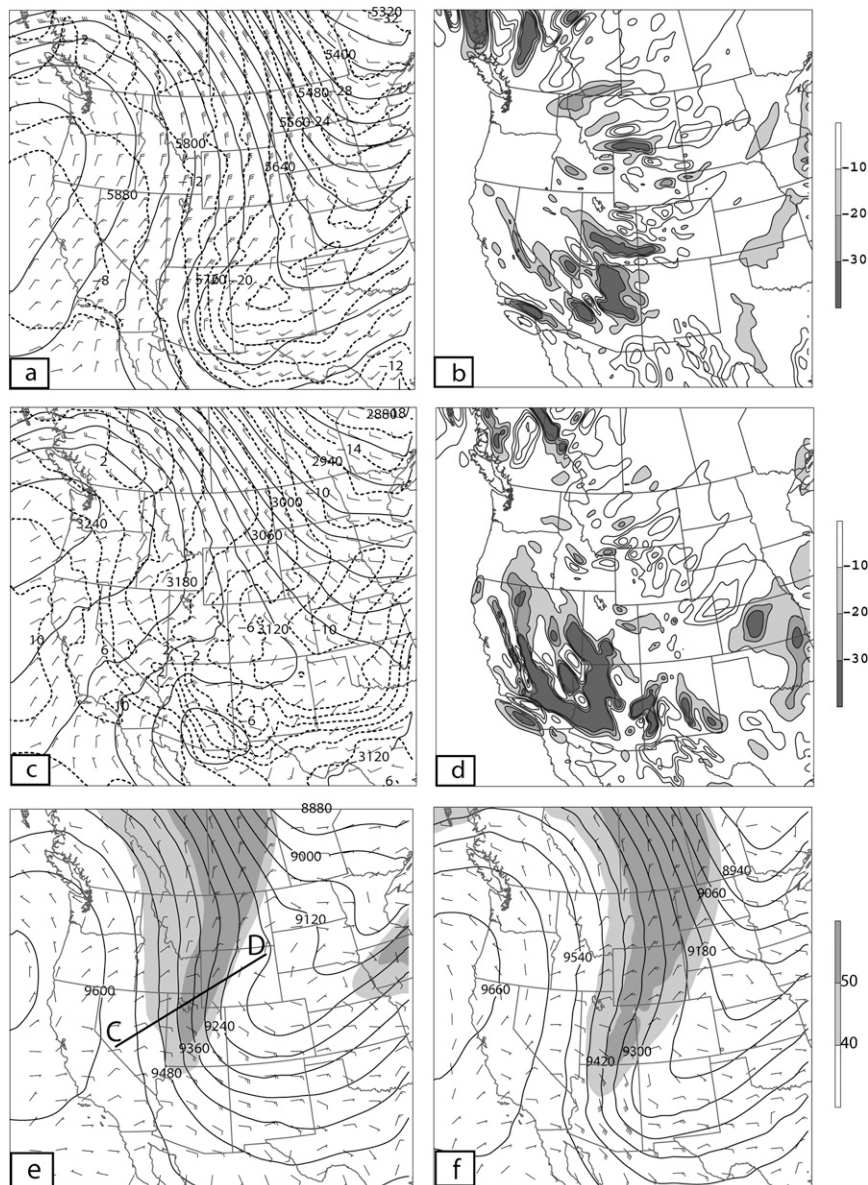
FIG. 13. (left) The 32-km NHMASS simulated geopotential height (solid; m), temperature (dashed; °C), and wind barbs and (right) the temperature advection by the total wind at (a),(b) 500 and (c),(d) 700 hPa valid at 1200 UTC 26 Oct 2003. Ageostrophic wind barbs, total wind speed (shaded; m s^{-1}), and geopotential height (solid; m) at 300 hPa valid at (e) 1800 UTC 25 Oct and (f) 0600 UTC 26 Oct 2003. Warm advection is denoted by solid contours and cold advection is shaded for values smaller than -10×10^{-5} K s^{-1}. Wind barb symbols are the same as in Fig. 5. Boldface line in (e) denotes cross-section location for Fig. 19b.

dry "spots" seemed to precede the big pool of dry air over north-central California (Fig. 15a), which were subsequently overrun by the main body of dry air (Fig. 15c) and separated from it (Fig. 15d). The following section will discuss possible sources of the dry air and associated drying processes occurring over these regions.

a. Sources of the dry air and the drying processes

Figure 16 denotes the 300-, 500-, and 700-hPa total wind and mixing ratio analyses from the 32-km NHMASS simulation valid at 1200 UTC 25 October (Figs. 16a,c, and e) and 26 (Figs. 16b,d, and f) October. One can see that in the upper and middle troposphere, a dry-air tongue
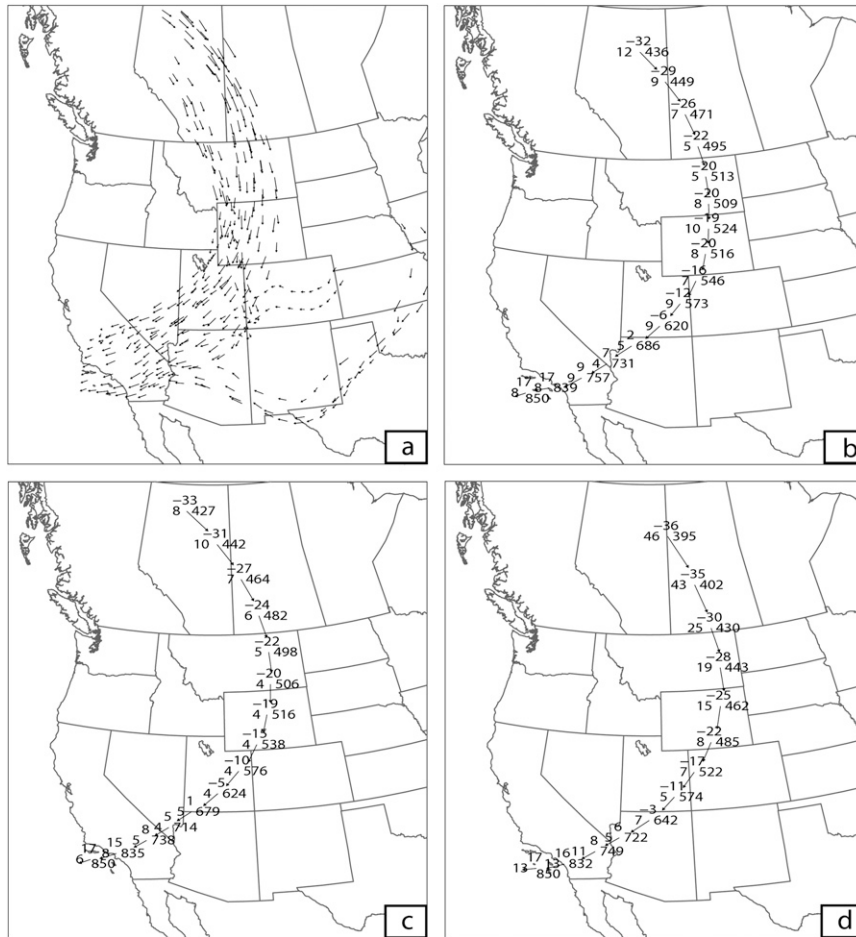
FIG. 14. Backward trajectories of (a) the winds for all 24 parcels, and the winds for parcels (b) A, (c) B, and (d) C from the 32-km NHMASS simulation starting at 0000 UTC 27 Oct 2003 back to their original positions at about 0300 UTC 25 Oct 2003. Trajectories are 3-hourly and caption is denoted below the figure: T is temperature (°C), RH is relative humidity (%), and P is pressure (hPa). Vectors denote winds with length proportional to wind speed.

moved southwestward from the central U.S.–Canada border to the southwestern United States (Figs. 16a–d). By 1200 UTC 26 October, this dry-air tongue has reached southern California and the nearby U.S.–Mexico border over Arizona (Figs. 16b and 16d). In the lower troposphere, a smaller dry spot preceded the main body of the dry air to its northeast (Fig. 16e) until it was overrun by the big dry pool from behind over southern California (Fig. 16f).

The upper-air mixing ratio pattern is similar to that at the surface in that they both appeared to have a main body that is preceded by a dry tongue or dry spots. Therefore, the main body of dry air near the surface and that in the upper air is likely one entity. The dry air reached the PBL over southern California likely through both horizontal advection by the prevailing

strong northeasterly winds at the northeast periphery of the high pressure ridge just off the western U.S. coast (Fig. 10), and vertical transport by the strong meso-α- to meso-β-scale subsidence, which phased over southern California (Figs. 12b, 12d, and 12f). The dry spots preceding the big dry-air pool in the lower level suggest that the first dry tongue has reached southern California before the main body arrived.

Figure 17 displays the RH and pressure on the 306-K isentropic surface. It clearly illustrates that at 1200 UTC 25 October, a dry tongue of RH < 20% beneath the 744-hPa pressure surface is over California with the driest air of RH < 10% beneath 840 hPa over northern and southern California, respectively while another massive, deeper dry-air pool is approaching the north-central
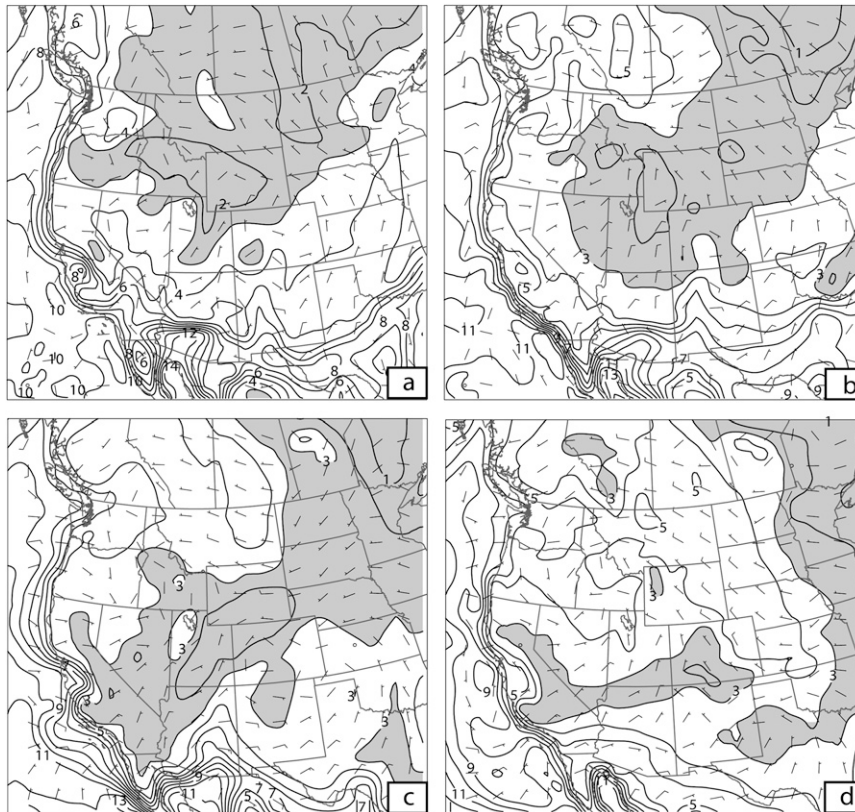
FIG. 15. Surface wind barbs and mixing ratios (g kg^{-1}; shaded for dry areas with values <3 g kg^{-1}) from the 32-km NHMASS simulation valid at (a) 1200 UTC 25 Oct, (b) 0000 UTC 26 Oct, (c) 1200 UTC 26 Oct, and (d) 0000 UTC 27 Oct 2003.

United States from southwestern Canada (Fig. 17a). The dry tongue over California lingered over this region from 0000 UTC 25 October to 0000 UTC 26 October (not shown) before being overrun by the massive dry air from behind (Fig. 17c). The shallowness of this dry tongue indicates that it is related to the dry PBL associated with the passage of the surface cold front (Fig. 2).

Figures 18a and 18b depict surface moisture flux divergence, 850-hPa isallobaric winds, and divergence caused by the isallobaric winds derived from the 8-km NHMASS simulation valid at 1500 UTC 25 October shortly after the surface cold front passed southern California. A maximum of moisture flux divergence persisted over southern California (Fig. 18a), which is related to the isallobaric wind adjustment behind the surface cold front (Fig. 18b). The persistent moisture divergence along the southern California coast caused the near-surface RH to remain below 20% even before the arrival of the main body of the dry air at about 1200 UTC 26 October, which is associated with the meso-α-scale subsidence caused by the secondary ageostrophic circulation in the exit region of the upper-level jet

streak. Such a twofold drying process results in extremely dry surface conditions, as described in section 2.

Based on the above analyses of the synoptic- to meso-α-scale environments, we can conclude that 1) the meso-α-scale subsidence in the exit region of an upper-level jet streak over the northwestern United States transported dry air in the mid- to upper troposphere toward the surface; 2) meanwhile, the strong mid- to upper-tropospheric northeasterly winds at the northeast periphery of a high pressure ridge that was just off the western U.S. coast advected the dry air southwestward toward the California coast; 3) the increasing curvature of the upper-level jet-front system and the strong cold-air advection over the southwestern United States strengthened the meso-α-scale subsidence; 4) the first dry-air surge within the PBL in southern California before 0000 UTC 26 October was caused by moisture divergence associated with the surface cold frontal passage; 5) the second dry-air tongue arrived in southern California around 1200 UTC 26 October as a result of prolonged horizontal advection and in-phase meso-α- to meso-β-scale subsidence throughout the troposphere.
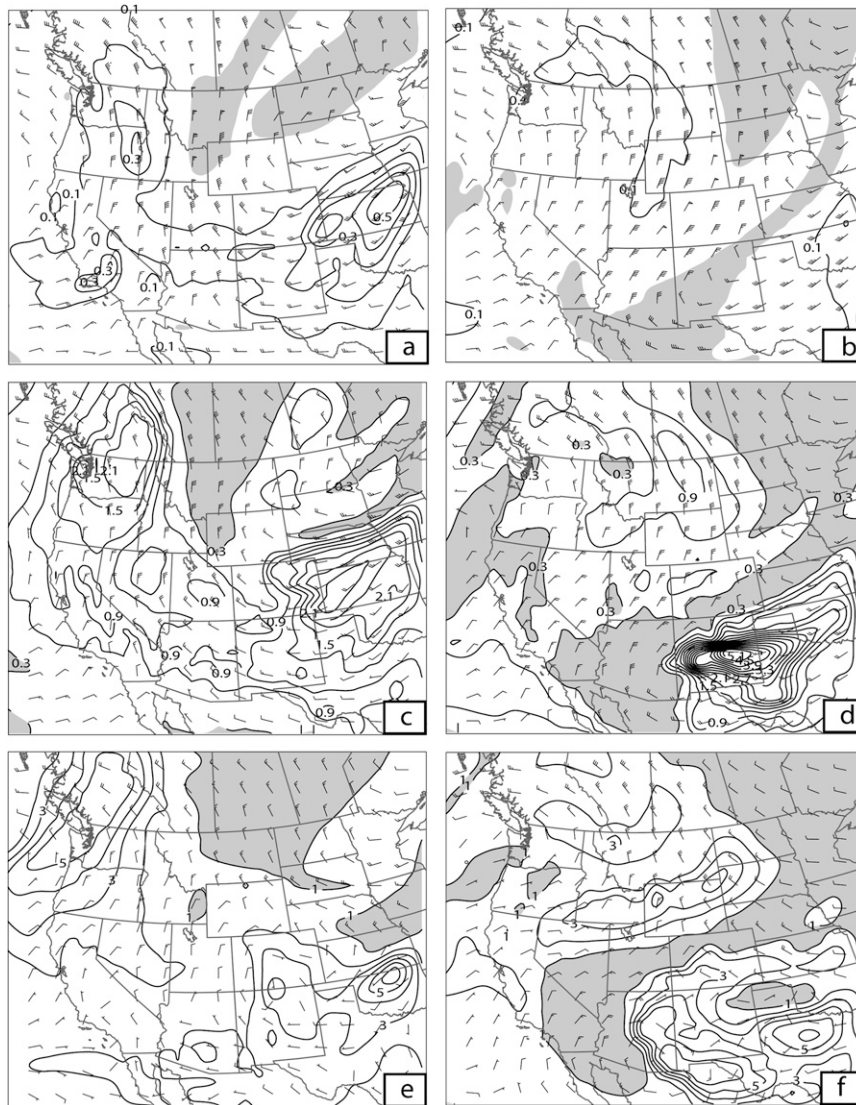
FIG. 16. (a),(b) 300-, (c),(d) 500-, and (e),(f) 700-hPa total winds and mixing ratios [shaded for dry areas with values smaller than 0.03 g (top panels), 0.3 (middle panels), and 1 g kg^{-1} (bottom panels)] from the 32-km NHMASS simulation valid at (left) 1200 UTC 25 Oct and (right) 1200 UTC 26 Oct 2003.

One might argue that the drying of the strong downslope winds, subsidence under the ridge, and suppression of the marine layer by the northeasterly flow may be sufficient to dry the air over the California and Arizona desert regions without needing to advect supplemental dry air thousands of kilometers from the northeast. This may just be speculation because our backward-trajectory analysis in the above section does not support this opinion. Rather, it shows that most of the parcels were from southwestern Canada and they did make an anticyclonic turn as they sank under the influence of the jet exit region.

The 32-km NHMASS NE–SW cross section analyses of wind speed, ageostrophic circulations, and potential temperatures show an interesting adjustment process in the exit region of the upper-level jet streak (Figs. 19a–c). At 0000 UTC 25 October, the jet streak is a nearly straight jet (Fig. 10a); therefore, a thermally indirect circulation is seen in the exit region with rising on the cold side to the northeast and sinking on the warm side to the southwest at 0300 UTC 25 October (Fig. 19a). However, as the curvature increases at 1800 UTC 25 October, the circulation pattern associated with the jet streak evolves from a four-cell pattern to a two-cell pattern due to the
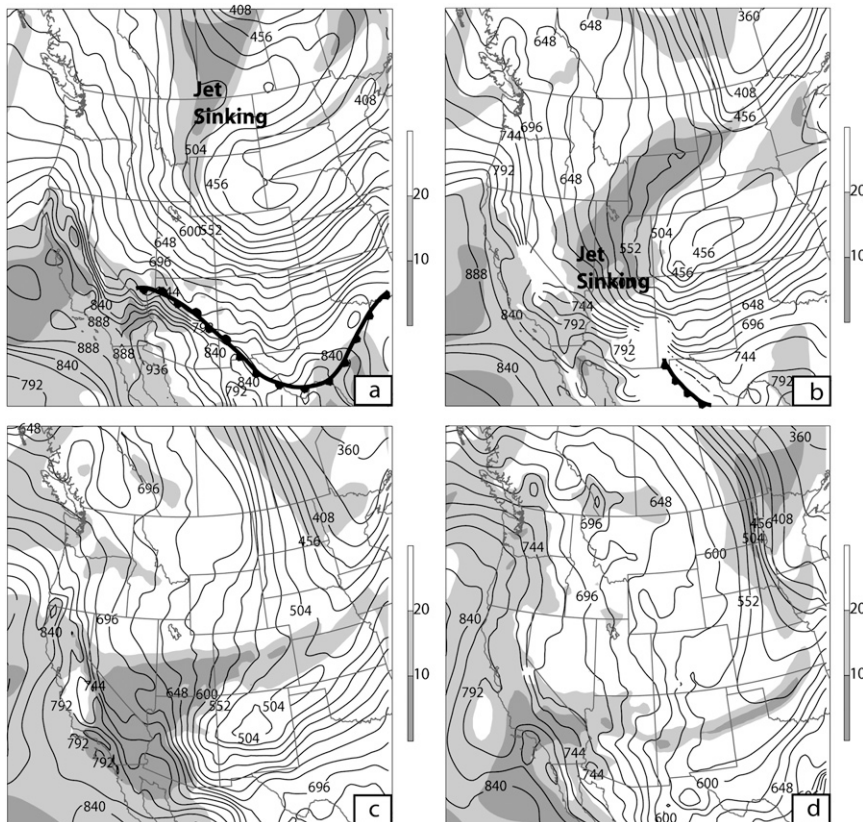
FIG. 17. Pressure (solid; hPa) and RH (shaded for dry areas with RH < 20%) projected on the 306-K isentropic surface from the 32-km NHMASS simulation valid at (a) 1200 UTC 25 Oct, (b) 0000 UTC 26 Oct, (c) 1200 UTC 26 Oct, and (d) 0000 UTC 27 Oct 2003.
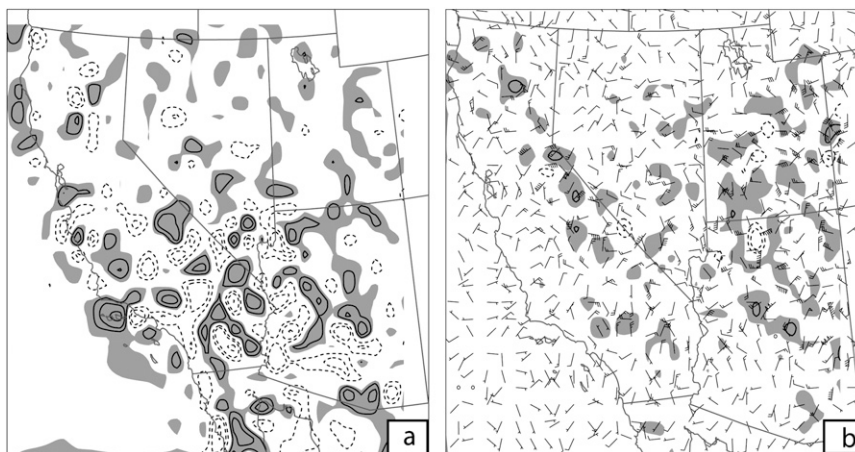

FIG. 18. (a) Surface moisture flux divergence and (b) 850-hPa isallobaric winds and associated velocity divergence from 8-km NHMASS simulation valid at 1500 UTC 25 Oct 2003. Moisture flux divergence (kg kg^{-1} s^{-1}) is shaded for values greater than 2×10^{-7} (dashed lines denote moisture flux convergence). Isallobaric wind divergence (s^{-1}) is shaded for values $> 1 \times 10^{-3}$. Wind barb symbols are the same as in Fig. 5.
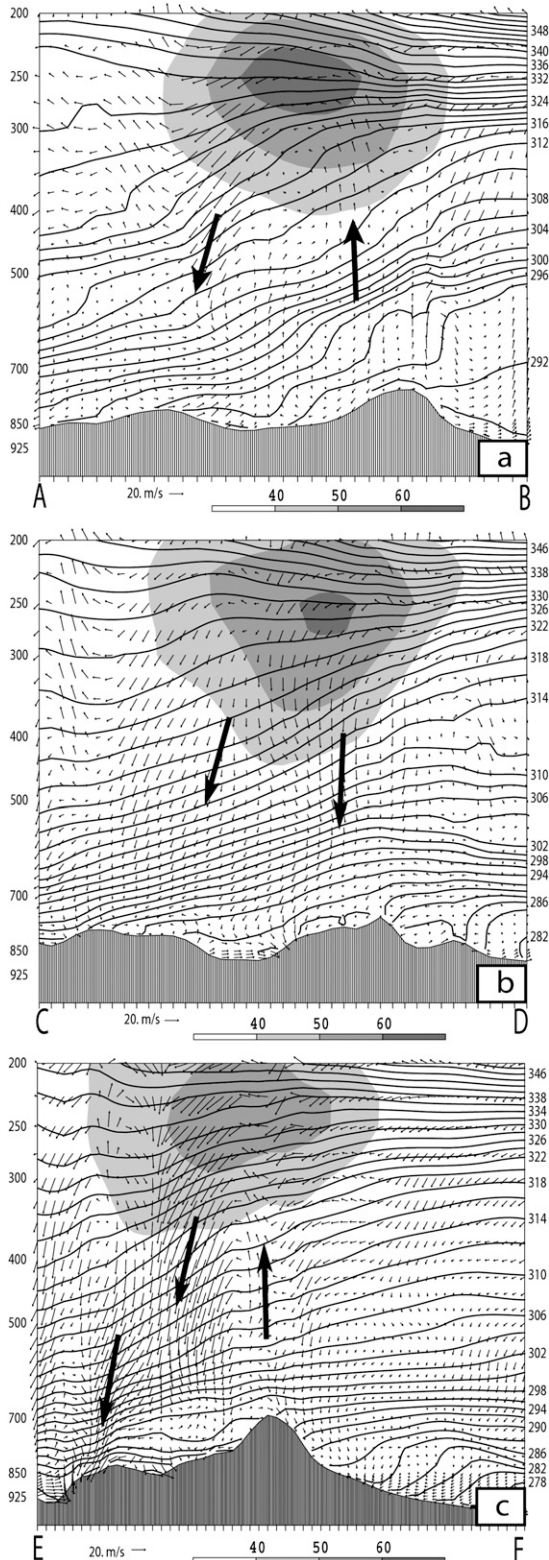
increasing nonlinear effects of the horizontal advection of kinetic energy along the flow (Uccellini and Johnson 1979; see Lin 2007 for a review); therefore, the downward motion dominates the exit region of the anticyclonically curved jet streak (Fig. 19b). Note that 18 h later, the sinking motion beneath the 300-hPa jet streak over the lee of the mountain peak of the Sawatch Mountain Range in the southern Rockies increases significantly and penetrates downward to about 700 hPa (Fig. 19c). There appears to be some wave activity on and above the jet streak level over the lee and beneath the jet streak level above the mountain peak (Fig. 19c). We will examine how the mesoscale wave activity near the coastal ranges affects the Santa Ana winds in the next section.

b. Generation of the severe downslope wind: A Santa Ana event

In the following section we will focus on the mesoscale dynamical processes over and just upstream from southern California to investigate the possible coupling mechanism between the meso-α-scale subsidence and lower-level environment, which likely induced the Santa Ana winds on the leeside of the coastal ranges.

Figure 20 indicates that the Santa Ana winds' occurrence is well simulated by the NHMASS modeling system. The surface pressure distribution in Fig. 20a denotes that high pressure developed in the Great Basin area as well as a low pressure system located in southern California and southwestern Arizona, similar to that in the observations depicted in Fig. 2. The primary surface wind near southern California was from the northeast. Such a surface pattern persists during the entire time period from 0000 UTC 25 October to 0000 UTC 27 October (not shown), which is consistent with an environment conducive to the occurrence of the Santa Ana events described in section 1 (Fig. 2).

Figures 20b and 20c show the 2-km NHMASS simulated surface wind barbs, temperature, and mixing ratios valid at 1200 and 2100 UTC 26 October. Strong northeasterly winds of 20 m s^{-1} prevailed along the coast northwest to Los Angeles as well as inland over southern California east of San Diego on the lee side of the coastal range and the nearby U.S.–Mexico border (Fig. 20b). A few small, dry "bubbles" with mixing ratio values less

---

←

FIG. 19. Vertical cross-section analysis of total wind speed (shaded, m s^{-1}, with winds heading off the page), ageostrophic circulations (vectors), and potential temperature (solid; K) from the 32-km NHMASS simulation valid at (a) 0300 UTC 25 Oct, (b) 1800 UTC 25 Oct, and (c) 1200 UTC 26 Oct 2003. Boldface arrows in (a),(c) denote the circulations. Locations of cross sections are denoted in Figs. 10a, 13e, and 10b.
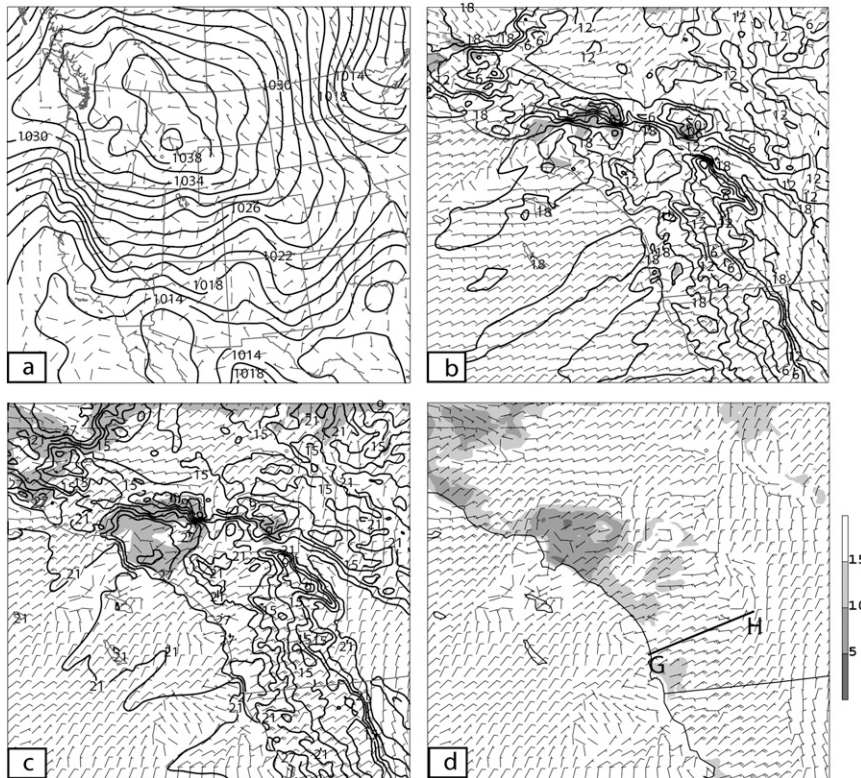
FIG. 20. (a) Sea level pressure (solid; hPa) and wind barbs at 1200 UTC 25 Oct 2003 from the 32-km simulation. (b) Surface mixing ratios (shaded for dry areas with values smaller than 2 g kg^{-1}), temperature (solid; °C), and wind barbs valid at 1200 UTC 26 Oct 2003 from the 2-km simulation. (c) As in (b) but at 2100 UTC 26 Oct 2003. (d) Surface RH (shaded for dry areas with RH < 15%) and wind barbs valid at 2100 UTC 26 Oct from the 2-km simulation. Wind barb symbols are the same as in Fig. 5. The boldface solid line in (d) denotes the location of the cross section in Fig. 21.

than 2 g kg^{-1} are evident on the downwind side of the coastal range, among which is a very small example near San Diego, downstream from the above-mentioned strong northeasterly winds. The temperature at this time along the southern California coast was between 18° and 21°C. As the daytime surface sensible heating increases, aided by the adiabatic warming accompanying the severe downslope wind, the afternoon temperature in this region climbed to higher than 27°C and the upstream wind speed increased to 25 m s^{-1} at 2100 UTC 26 October (Fig. 20c). The warming caused the surface RH to remain below 15% even though the surface mixing ratio had increased to above 2 g kg^{-1} (Fig. 20d).

Cross-section analyses of the potential temperature, RH, and ageostrophic circulation vectors (Figs. 21a and 21b), the Brunt–Väisälä frequency squared (N^2) (Figs. 21c and 21d), and the bulk Richardson number (Ri), as well as ageostrophic circulation vectors (Figs. 21e and 21f) from the 8-km NHMASS simulation, reveal that there was an early dry tongue on the lee side of the

coastal range due to isallobaric adjustments associated with the cold front (Fig. 21a), before the extremely dry air (RH < 5%) from the meso-α- to meso-β-scale subsidence under the jet exit region reached the PBL (Fig. 21b). Very strong downslope winds of velocity greater than 30 m s^{-1} near the surface are seen to develop on the lee side (Fig. 21b). Also evident are the overturning isentropes in the 850–750-hPa layer with an Ri < 0.25 in a region on the lee side characterizing wave breaking and strong turbulent mixing (Figs. 21e and 21f). The lower troposphere was statically stable everywhere except in the vicinity of the wave breaking zone (Figs. 21c and 21d), which indicates strong turbulent mixing there. The wave breaking region can act as an internal boundary, according to the resonant amplification mechanism, which reflects the wave energy back to the ground and produces a high-drag state through partial resonance with the upward-propagating mountain waves (Clark and Peltier 1984; see Lin 2007 for a review).
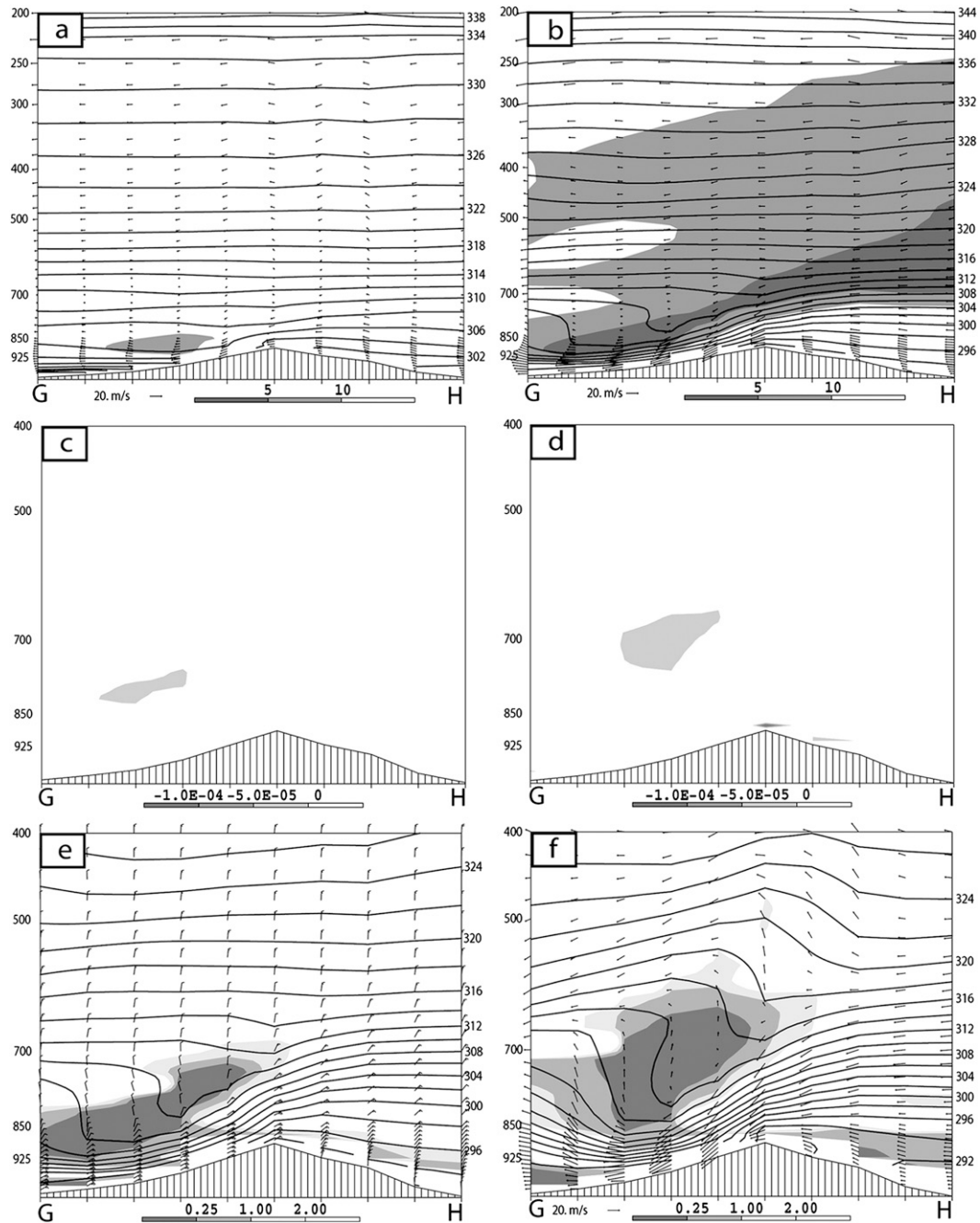
FIG. 21. Cross-section analyses along GH (denoted in Fig. 20d) from the 8-km simulation of RH (%, shaded for RH < 10%), circulations (vectors), and θ (solid; K) valid at (a) 1800 UTC 25 Oct and (b) 1000 UTC 26 Oct 2003. Here, N^2 (shaded for values $< -5 \times 10^{-5}$ s^{-2}) are valid at (c) 1000 UTC 26 Oct and (d) 1800 UTC 26 Oct 2003. (e) The Ri (shaded for value <2), θ, and wind barbs valid at 1000 UTC 26 Oct and (f) the Ri, θ, and circulations (vectors) valid at 1800 UTC 26 Oct 2003. Wind barb symbols are the same as in Fig. 5.

Figure 21e also indicates that a local wind reversal level exists in the vicinity of the wave breaking region at about 750 hPa. For a stationary mountain wave (phase speed $c = 0$), this wind reversal level coincides with the critical level (where the phase speed and basic wind speed are equal) and thus is called a wave-induced critical level. This critical level, with the Ri number being smaller than 0.25, may reflect or even overreflect the wave energy back to the ground. The overreflected wave may be in phase, or partially in phase, with the

upward-propagating mountain waves; therefore, wave instability may develop, thus contributing to the development of severe downslope winds over the lee side (Lin 2007), as seen in Fig. 21. Later, at the above cross section, the wave breaking zone is seen to expand upward to ~600 hPa and some weak hydraulic jumps have developed over the mountain peak and downstream over the lee side (Fig. 21f). The hydraulic jump develops as a result of the flow regime at the upwind side, which transitioned from a subcritical state to a supercritical state (Smith 1985; see Lin 2007 for a review). The wave breaking region expanded likely due to the wave duct that is supported by the critical level.

An animation of the cross-section analyses of RH, circulation, and potential temperature (not shown) suggests that the wave-induced critical level phased with the upstream descending dry tongue under the exit region of the upper-level jet streak at 1000 UTC (0200 LST) 26 October to transport and mix down the extremely dry air to the PBL over the lee side. The high momentum from the jet streak accentuated the flow on the upwind side and its subsequent transition from a subcritical state to a supercritical state as well as increasing the vertical wind shear on the lee side, thus contributing to the formation of the severe downslope winds. The role of the meso-α-scale subsidence is to transport the extremely dry air from the upper troposphere toward the surface as well as to warm up the air column through adiabatic compression.

The severe downslope winds passed through the canyons and warmed adiabatically. When reaching the flatter plains, the winds become hot, very dry, and gusty. The severe downslope wind in southern California is also known as the Santa Ana wind. Once the Santa Ana wind develops, hazardous fire weather conditions are anticipated. Figure 22 shows the skew T–log$p$ thermodynamic diagrams at Miramar as simulated by the 8-km NHMASS model valid at 1800 UTC 25 October (Fig. 22a) and 1000 UTC 26 October (Fig. 22b). A nocturnal temperature inversion is evident in both soundings due to the diabatic cooling at the surface after sunset. The temperature and dewpoint profiles at these times depict a dramatic drying of the lower troposphere between 800 and 950 hPa, especially at 1000 UTC 26 October at the 900-hPa level when the dewpoint depression increased to 43°C. As discussed above, the unusual drying process is likely due to the phasing of the wave-induced critical level and the descending dry air tongue from the meso-α- to meso-β-scale subsidence associated with the upper-level jet streak.

We can summarize the above discussion of the mesoscale environments as follows: 1) Santa Ana wind occurrence is simulated reasonably well by the NHMASS

modeling system, 2) a wave breaking region in the lower troposphere on the lee side of the coastal range acted as an internal reflecting boundary to reflect the mountain wave energy back to the ground and created the severe downslope winds through partial resonance with the upward-propagating mountain waves and the hydraulic jump mechanism, 3) a wave-induced critical level coupled with the upstream dry air tongue from the meso-α- to meso-β-scale subsidence to transport and mix down the extremely dry air to the PBL on the lee side, and 4) the high momentum from the jet streak plays a role in this process by increasing the kinetic energy of the flow on the upwind side as well as the shear instability on the lee side of the mountain.

5. Summary and conclusions

In this study both observational data and numerical simulations have been employed to diagnose the synoptic-through mesoscale atmospheric environments conducive to forest fires during the October 2003 extreme fire event in southern California.

The synoptic-scale environment that is evident in the observations includes an intensifying upper-level high pressure ridge just off the northwestern U.S. coast, an upper-level jet streak on its northeast periphery, and a downstream deepening trough over the north-central United States. The mesoscale environment in southern California near San Diego, as simulated in the numerical model, is favorable for the development of severe downslope winds where a wave breaking region in the lower troposphere on the lee side of the coastal range acted as an internal reflecting boundary to redirect the mountain wave energy back to the ground, which created the severe downslope winds through partial resonance with the upward-propagating mountain waves. The synoptic-scale and the mesoscale environments are coupled together to bring the extraordinary dry air from the upper troposphere to the planetary boundary layer to create a favorable environment for the human-caused forest fires to grow uncontrollably. The coupling between the synoptic-scale and mesoscale environments can be summarized as a three-stage process depicted in the schematics in Figs. 23a–c.

During stage I, the meso-α-scale subsidence of the transverse ageostrophic circulation in the jet exit region transported dry air in the mid- to upper troposphere toward the surface. As a result of adiabatic compression the dry air warms up as it sinks and surface pressure rises under the converging flow aloft. The first dry air surge arrived in southern California within the PBL before 0000 UTC 26 October as a result of moisture divergence and isallobaric adjustments behind the surface cold front.
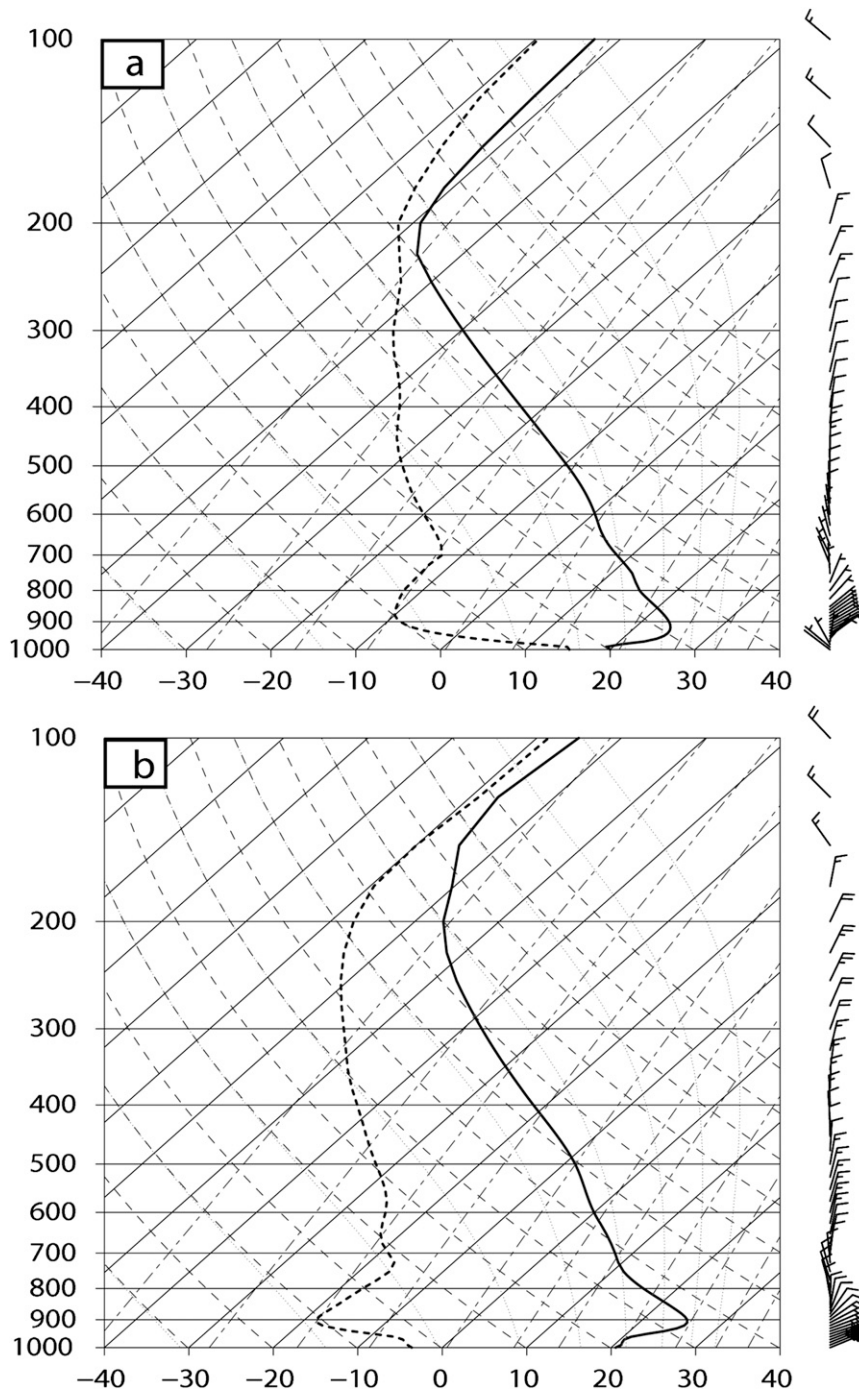
FIG. 22. Thermodynamic diagrams of temperature (solid) and dewpoint temperature (dashed) and the wind profile at KNKX valid at (a) 1800 UTC 25 Oct and (b) 1000 UTC 26 Oct 2003 from the 8-km NHMASS simulation.

The isallobaric wind increases as a result of the integrated pressure rising behind the surface cold front. Isallobarically induced moisture divergence was a factor in drying the air behind the cold front as well as forcing subsidence and a thermally direct ageostrophic circulation behind the

low-level cold front. The mid- to upper-level and lower-level dry air was not in phase at this stage.

During stage II, the anticyclonic curvature of the jet streak increased and the strong northeasterly winds in the exit region advected the dry air southwestward
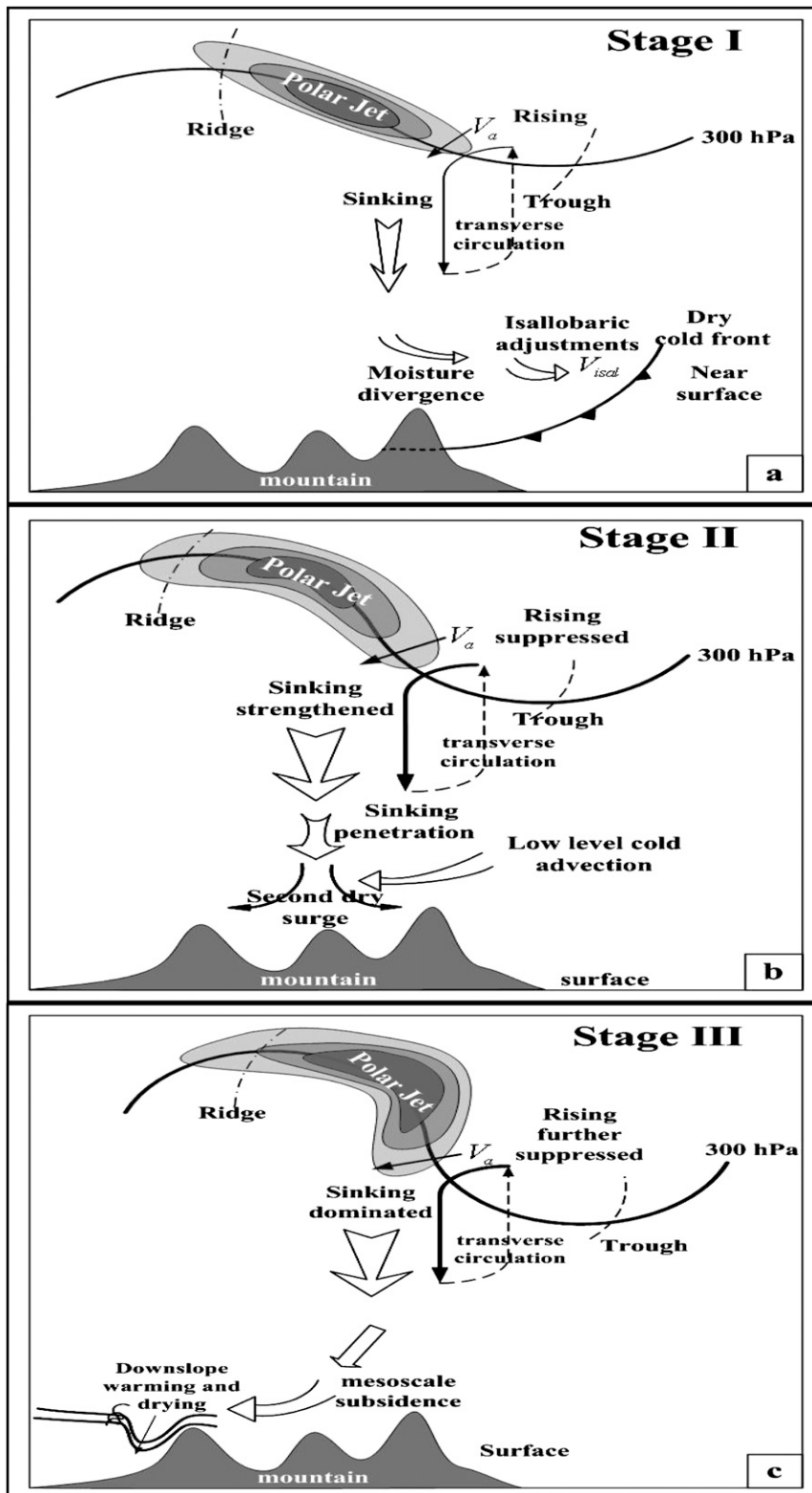
FIG. 23. Stages (a) I, (b) II, and (c) III of a three-stage adjustment process within the exit region of an upper-level jet streak.

toward the California coast. The curvature of the jet streak and the strong cold-air advection over the southwestern United States strengthened the meso-α- to meso-β-scale subsidence over these regions. The upper-level sinking motions penetrated down to the lower troposphere over southern California and northeastern Arizona around 1200 UTC 26 October. The second dry-air tongue reached southern California as a result of prolonged horizontal advection and strong mesoscale subsidence but at that time it did not directly couple to the dry-air region behind the surface dry cold front.

During stage III, a wave-induced critical level coupled with the upstream dry tongue from the meso-α- to meso-β-scale subsidence (in stage II) to transport the extremely dry air to the PBL on the lee side of the coastal range near San Diego. Wave breaking and strong turbulence acted as an internal boundary to reflect the mountain wave energy back to the ground, led to the formation of a hydraulic jump, and created Santa Ana winds. The very dry, hot, and gusty conditions near the surface in southern California pose a great danger for the potential erratic development of major blow-up fires.

REFERENCES

Brotak, E. A., and W. E. Reifsnyder, 1977a: An investigation of the synoptic situations associate with major wildland fires. *J. Appl. Meteor.,* **16,** 867–870.

——, and ——, 1977b: Predicting major wildland fire occurrence. *Fire Management Notes,* **38** (3), 5–8.

Byram, G. M., 1954: Atmospheric conditions related to blow-up fires. Southeastern Forest Experiment Station Paper 35, USDA Forest Service, Asheville, NC, 42 pp.

Clark, T. L., and W. R. Peltier, 1984: Critical level reflection and the resonant growth of nonlinear mountain waves. *J. Atmos. Sci.,* **41,** 3122–3134.

Durran, D. R., 1990: Mountain waves and downslope winds. *Atmospheric Processes over Complex Terrain, Meteor. Monogr.,* No. 45, Amer. Meteor. Soc., 59–81.

Eliassen, A., and E. Palm, 1960: On the transfer of energy in stationary mountain waves. *Geofys. Publ.,* **22,** 1–23.

Glickman, T., Ed., 2000: *Glossary of Meteorology.* 2nd ed. Amer. Meteor. Soc., 855 pp.

Holton, J. R., 2004: *An Introduction to Dynamic Meteorology.* 4th ed. Elsvier, 535 pp.

Johnson, D. L., 2004: Southern California wildfires October 20 to November 3, 2003. NOAA/NWS Service Assessment, Silver Spring, MD, 45 pp.

Kaplan, M. L., Y.-L. Lin, J. J. Charney, K. D. Pfeiffer, D. B. Ensley, R. P. Weglarz, and D. S. DeCroix, 2000: A terminal area PBL prediction system at Dallas-Fort Worth and its application in simulating diurnal PBL jets. *Bull. Amer. Meteor. Soc.,* **81,** 2179–2204.

Klemp, J. B., and D. K. Lilly, 1975: The dynamics of induced Downslope winds. *J. Atmos. Sci.,* **32,** 320–339.

Kondo, J., and T. Kuwagata, 1992: Enhancement of forest fires over northeastern Japan due to atypical strong dry wind. *J. Appl. Meteor.,* **31,** 386–396.

Lin, Y.-L., 2007: *Mesoscale Dynamics.* Cambridge University Press, 630 pp.

MESO, Inc., 1994: MASS version 5.6 reference manual. MESO Inc., Troy, NY, 118 pp. [Available from MESO Inc., 185 Jordan Rd., Troy, NY 12180.]

Raphael, M. N., 2003: The Santa Ana winds of California. *Earth Interactions,* **7.** [Available online at http://EarthInteractions.org.]

Schaefer, V. J., 1957: The relationship of jet streams to forest wildfires. *J. For.,* **119,** 419–425.

Small, I. J., 1995: Santa Ana winds and the fire outbreak of fall 1993. NOAA Tech. Memo. NWS WR-230, 15 pp.

Small, R. T., 1957: The relationship of weather factors to the rate of spread of the Robie Creek fire. *Mon. Wea. Rev.,* **85,** 1–8.

Smith, R. B., 1985: On severe downslope winds. *J. Atmos. Sci.,* **42,** 2597–2603.

Uccellini, L. W., and D. R. Johnson, 1979: The coupling of upper- and lower-tropospheric jet streaks and implications for the development of severe convective storms. *Mon. Wea. Rev.,* **107,** 682–703.